Development of the NRIPR Mesoscale Meteorological Model at Eötvös University

Master Thesis

András Zénó Gyöngyösi

Spring 2000

Contents

List of Tables

List of Figures

Chapter 1

Introduction

Environmental protection is becoming a more serious and intensively researched area in Hungary, East Europe. This research includes quantitative forecasts of the concentrations of gaseous and aerosol contaminants. Since the Gaussian plume model has shortcomings, especially over complex terrain [Pielke, 1984], mesoscale meteorological models are needed for more accurate estimation of the mesoscale air quality. In addition, mesoscale models are frequently used in many other fields.

Mesoscale systems can be phenomenologically defined as meteorological features too gross to be observed from a single station, yet too small to appear even on a sectional synoptic chart [Ligda (1951)]. This implies that the horizontal scale ranges from a few kilometers to several hundreds of kilometers with a time-scale of 1 to 12 hours or so. The vertical scale extends from tens of meters to the depth of the troposphere. Using scale analysis [e.g., Orlanski, 1984], we make a more formal definition:

- The horizontal scale must be sufficiently large so that the hydrostatic. equation can be used
- The horizontal scale must be sufficiently small so that the Coriolis term is small (although it can still be significant!) relative to the advective and pressure gradient forces, resulting in a flow field that is substantially different from the gradient wind relation, even in the absence of friction effects.

Mesoscale phenomena that have horizontal scales of 20–200 km [aspect ratios of $\mathbf{O}(10)$ L_H/L_Z 10] are largely hydrostatic, are affected by the earth's rotation, and have substantial ageostrophic components. Included in this category are convective storm ensembles, frontal and jet stream phenomena, some orographic flows (lee cyclogenesis), polar lows, coma clouds, intensive extratropical storms (bombs), valley winds, sea breeze circulations and the morning glory [Emanuel, 1983]. Standardization of atmospheric flows based on scale analysis of Orlanski was arbitrary and ill-defined [Orlanski, 1975]. Pielke (1975) places the upper limit of mesoscale to Orlanski's Meso-β, while Stull (1988) defines the lower bound of it at Micro-α. In addition, todays non-hydrostatic mesoscale models are able to simulate even meso-γ and Micro-α motions [Thunnis and Bornstein, 1997]. Recently, Thunnis and Bornstein (1997) proposed new time and space scale boundaries, including the following three changes to Orlanski's scale classification:

1. Renaming Meso-α to Macro-γ
2. Renaming Micro-α to Meso-δ
3. Introducing a Micro-δ subclass

The first two changes shift mesoscale down into smaller scale motions. They gave a dynamically based definition for mesoscale:

> "Organized atmospheric motions with Coriolis force large enough to determine rotational direction but small enough to be assumed latitude independent; motions originate in troposphere."

In addition, they gave an exact terminology of the different scale vertical movement:

diffusion Random turbulent motion with zero mean vertical velocity.

convection Organized non-hydrostatic vertical movement, which has the same order of magnitude as the horizontal motion, can be both thermal (free) or mechanical (forced), and produce the horizontal motion by continuity.

advective circulation Organized mesoscale circulation cells, in which horizontal convergence result in vertical motions at least one order smaller velocities as the horizontal.

In general two main types of mesoscale systems are known: terrain induced and synoptically induced systems [Pielke, 1984]. There are two kind of approaches to simulate mesoscale systems:

1. Mesoscale models of severe meteorological phenomena
2. Mesoscale circulation models

Examples of the first approach are models of severe storms, which are mostly based on General Circulation Models (GCMs). Mesoscale circulation models are well suited to simulate mild phenomena as land-sea breezes or mountain winds. These models have been developed independently from GCMs [Kondo, 1989]. There are some models which are able to simulate both kinds of phenomena with one model [e.g., Anthes and Warner, 1978], but parameterizations in the model are much different for two phenomena.

Mesoscale systems initiated by atmospheric instability, usually occur less frequently at a given location and, because they are not forced by well-defined geographic features, the data requirement of these phenomena is more formidable [Pielke, 1984]. A large percentage of rainfall over the Earth results from such features.

One of the first numerical studies of sea- and land-breezes was a two dimensional model of Estoque (1961). McPherson (1970) was the first to investigate land-sea breeze in a three dimensional simulation, and was followed by many others.

Nocturnal drainage flow or katabatic wind [e.g., Manins and Sawford, 1978], which is a three dimensional phenomenon, was numerically simulated by Yamada (1981), for example. Mahrer and Pielke (1977) demonstrated differences in depth and strength of upslope and downslope winds in the absence of a prevailing synoptic flow. They reported that the flow tends to form a closed circulation, so that if pollutants were continuously released in one segment of the flow, they would tend to accumulate. Such *recirculation* is ignored in the Gaussian plume models [Pielke, 1984].

As it will be discussed more precisely later, mesoscale models (for economical purposes) are usually integrated over a portion of the globe on a limited area, thus correctly formulated boundary conditions are essential. Such questions have been discussed by Oliger and Sundström (1976) (with respect to the lateral boundaries) by Klemp and Lilly (1975) (with respect to the top boundary) and by many others. A tutorial of the lateral boundary formulation of Limited Area Models was given by Warner *et al.* (1997). Another important question is the closure problem, i.e., the prognostic equations of a turbulent variable contain second order moments that can be predicted with the use of third order moments, and so on. To close the set of equations, different techniques were reported in Mellor and Yamada's paper (1974) or by Wyngaard (1980), for example.

Initialization on the mesoscale is also problematic. Normal mode initialization is difficult, but not impossible [Briere, 1982] to apply, because the normal modes cannot be determined readily for complicated boundary conditions. Dynamic initialization is preferred, which does not require normal mode decomposition.

The objective of this paper is the adaptation of a three-dimensional hydrostatic first order closure mesoscale circulation limited area model, which was developed for the assessment of CO_2 and water vapor concentrations for a certain region in the atmosphere. The Hungarian version has been developed and tested. In the next section a brief description of the considered model will be given. In chapter 2 the adaptation of this model will be described. Section 2.2 will provide the evaluation of the model with respect to the topography, and Section 2.3 will summarize the works on the landuse–land cover datasets. In this paper a limited number of figures of the model outputs are presented; others are only referred to. All diagrams of the model outputs can be found in the log-book of the model runs available in printed form, from the Department of Meteorology, Eötvös University, Budapest, Hungary, or in downloadable compressed POSTSCRIPT files through anonymous File Transfer Protocol (FTP).

Chapter 2

Model Description

In this chapter only a description of the model equations is given; derivations are only referred to if necessary.

This mesoscale model has been developed at NRIPR[1], Japan, during the past 20 years by Kondo *et al.* The main purpose of this project was to develop a more powerful system than Gaussian type models to study and forecast transport and diffusion processes of pollutants. If we want to assess the concentration of a pollutant in the atmosphere which interacts with it's environment, we need to know the time variation of the variables in the atmosphere (e.g., wind, temperature, etc). If we simply interpolate these variables from large-scale data, we lose a lot of information about the interaction of the atmosphere and the surface, a very important feature in the description of pollutant transport processes. This model is a coupled mesoscale meteorology and air quality model, which can calculate meteorological variables and obtain pollutant concentrations simultaneously.

2.1 Governing equations of the model

The governing equations can be derived from the basic conservation laws for mass, momentum and heat. In addition equations for some gaseous contaminants are solved. In this mesoscale circulation model, the simulated phenomena have a vertical scale which is much less than the scale depth of the atmosphere[2] (H). In addition, wind velocity magnitude is much smaller than the speed of sound in the atmosphere. For these reasons, mass conservation can be considered through the so-called shallow continuity equation or non-divergent assumption:

$$div\mathbf{V} = \frac{\partial u}{\partial x} + \frac{\partial v}{\partial y} + \frac{\partial w}{\partial z} = 0 \qquad (2.1)$$

where u,v,w are the components of wind velocity vector $\mathbf{V}$ in the Cartesian coordinate system. This assumption ignores spatial variation for density and filters sound waves from the model.

Conservation of momentum is considered in the prognostic equations of the horizontal wind velocity components. They can be written as follows:

$$\frac{\partial u}{\partial t} = -u\frac{\partial u}{\partial x} - v\frac{\partial u}{\partial y} - w\frac{\partial u}{\partial z} + fv - \frac{1}{\varrho}\frac{\partial p}{\partial x}$$

$$\frac{\partial v}{\partial t} = -u\frac{\partial v}{\partial x} - v\frac{\partial v}{\partial y} - w\frac{\partial v}{\partial z} - fu - \frac{1}{\varrho}\frac{\partial p}{\partial y}$$

where ϱ is the average density of the air (now treated as constant through the incompressible assumption Eqn 2.1) and f is the Coriolis parameter ($2\Omega\sin\phi$ put equal to 10^{-4} s^{-1}). Assuming geostrophic synoptic-scale wind, and introducing the mesoscale scaled pressure[3] the governing equa-

[1] National Research Institute for Pollution and Resources, forerunner of todays National Institute of Resource and Environment (NIRE)

[2] Scale depth of the atmosphere is defined as:

$$H := \frac{1}{\alpha_0}\frac{\partial \alpha_0}{\partial z}$$

[3] or Exner function defined:

$$\pi := c_p(\frac{p}{p_{00}})^{R_d/c_p}$$

tions are as follows:

$$\frac{\partial u}{\partial t} = -u\frac{\partial u}{\partial x} - v\frac{\partial u}{\partial y} - w\frac{\partial u}{\partial z} - \Theta\frac{\partial \pi}{\partial x} + f(v - v_g)$$

$$\frac{\partial v}{\partial t} = -u\frac{\partial v}{\partial x} - v\frac{\partial v}{\partial y} - w\frac{\partial v}{\partial z} - \Theta\frac{\partial \pi}{\partial y} - f(u - u_g)$$

where

$$(u_g, v_g) := \frac{1}{f\varrho}(-\frac{\partial p}{\partial x}, \frac{\partial p}{\partial y})$$

is the geostrophic wind, and

$$\Theta = T(\frac{p_{00}}{p})^{R_d/c_p}$$

is the large-scale average potential temperature. These equations are valid for the instantaneous values if the wind speed is much smaller than the speed of light. We cannot give initial values for turbulent flow, so we have to solve the equations for the mean[4] values, cut-off the deviations and parameterize the effect of turbulence as divergence of kinematic momentum flux using the K-theory (a first order closure). These assumptions yield

$$\frac{\partial u}{\partial t} = -u\frac{\partial u}{\partial x} - v\frac{\partial u}{\partial y} - w\frac{\partial u}{\partial z} - \Theta\frac{\partial \pi}{\partial x} + f(v - v_g) - \frac{\partial}{\partial x_i}K_M\frac{\partial u}{\partial x_i} \quad (2.2)$$

$$\frac{\partial v}{\partial t} = -u\frac{\partial v}{\partial x} - v\frac{\partial v}{\partial y} - w\frac{\partial v}{\partial z} - \Theta\frac{\partial \pi}{\partial y} - f(u - u_g) - \frac{\partial}{\partial x_i}K_M\frac{\partial v}{\partial x_i} \quad (2.3)$$

Using the hydrostatic assumption and Boussinesq approximation, the third equation of motion can be written simply as:

$$\frac{\partial \pi}{\partial z} = \frac{g\theta}{\Theta^2} \quad (2.4)$$

where R_d is specific gas constant for dry air, c_p is specific heat capacity at constant pressure and $p_{00} = 1000$ mbar. The Exner function can be split into large-scale average and mesoscale perturbations. Here only the perturbation is considered, and π denotes the mesoscale deviation of the scaled pressure

[4] mean refers to grid volume and time average, using Reynold's averaging rules:

$$\frac{\int_t^{t+\Delta t}\int_x^{x+\Delta x}\int_y^{y+\Delta y}\int_z^{z+\Delta z}(\,)\,dt\,dx\,dy\,dz}{\Delta t\,\Delta x\,\Delta y\,\Delta z}$$

Here θ is the mesoscale potential temperature deviation. Note that the mesoscale pressure gradient has opposite sign to the buoyancy term $g\theta/\Theta^2$, in contrast to the synoptic scale pressure gradient, which has the same sign as the gravity force. See Appendix A.1 for the complete derivation of the hydrostatic equation (Eqn 2.4).

The prognostic equation for temperature can be derived from the First Law of Thermodynamics. The derivative of potential temperature can be split into local derivative and advection terms. To describe advection in the turbulent flow, turbulent heat flux divergence contributes to the time variation of potential temperature in addition to diabatic effects such as heat flux divergence, the latent heat of any phase change and anthropogenic heat, for example. The prognostic equation for potential temperature can be written as:

$$\frac{\partial \theta}{\partial t} = -u\frac{\partial \theta}{\partial x} - v\frac{\partial \theta}{\partial y} - w\frac{\partial \theta}{\partial z} - \frac{\partial}{\partial x_i}K_H\frac{\partial \theta}{\partial x_i} + \frac{1}{c_p\varrho}Q_s + \frac{1}{c_p\varrho}LE \quad (2.5)$$

where Q_s denotes sensible heat transfer by diabatic processes and L is the latent heat associated with the phase change E.

For any gaseous pollutant we have to solve the transport equation, formally very similar to the equation for temperature (Eqn 2.5), with net body source and sink terms. Wind field and parameterizations of subgrid fluxes are obtained from the simultaneously calculated meteorological variables.

To assure the flow is parallel to the terrain at the lower boundary, it is convenient to introduce a new vertical coordinate (s) as Mannouji (1982) suggested:

$$s := \frac{z - z_G}{D} \quad (2.6)$$

where z_G is the altitude of the terrain, $D := z_T - z_G$, where z_T is the height of the model domain. For the numerical solution the vertical grid is assumed in a variable resolution, nearly logarithmic, with a finer grid near surface, which gives a grid network as presented on Figure 2.1 in an east-west cross-section of the model domain (left) and the concordance of vertical indices to real height is also shown (right). With this new vertical coordinate, the model equations are transformed into a terrain following coordinate system. See Appendix A.2 for the terrain following governing equations. Wong and Hage (1983) pointed out that this kind of coordinate transformation gives the exact equation system in case of

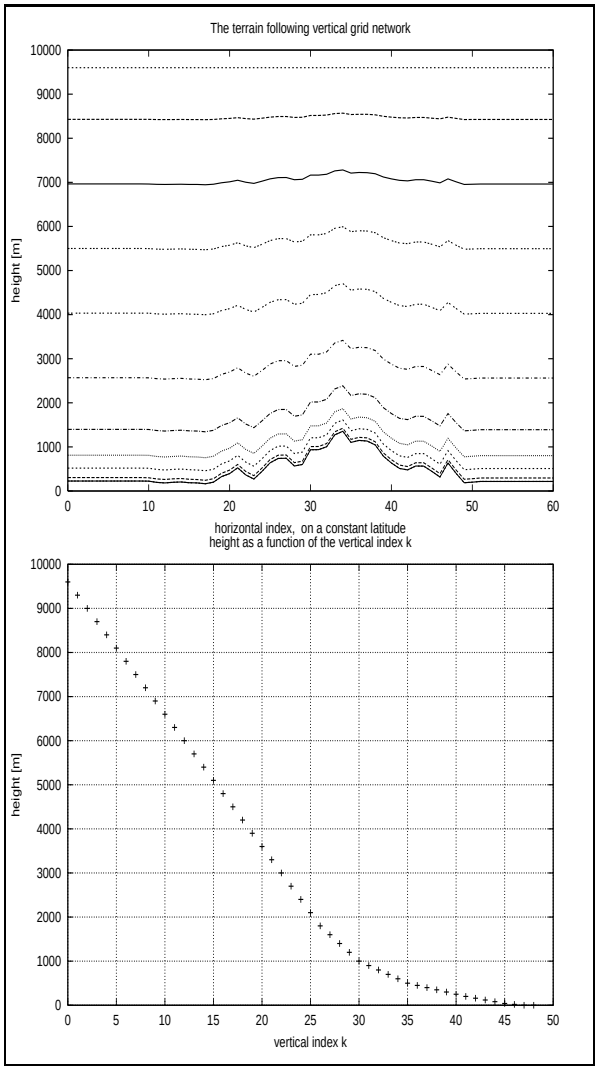

Figure 2.1: **The vertical grid network**

small vertical acceleration, so this transformation is valid in the hydrostatic assumption, even for significant slope angle [Yoshizaki, 1988]. Eqns (A.4)-(A.8) are the basic governing equations for this mesoscale model.

2.2 Boundary conditions

The model domain is limited both in vertical and horizontal directions, i.e., it has top, lateral and bottom boundaries. Only the last one has physical meaning, the others are introduced only for computational necessity. Usually, a greater number of boundary conditions are used than required by the model equations. As Oliger and Sunström (1976) pointed out, conservation relations that are represented in a non-dissipative approximation (e.g., leap-frog) and that are overspecified, generate short waves at the boundary that propagate into the model domain with the fastest wave speed permitted. Oliger and Sundström found that hydrostatic models are ill-posed for any local[5] boundary conditions, and some erroneous waves are expected to be created at the boundaries in such a model. Some modelers are using an upstream scheme near the lateral boundaries to dampen such noises [e.g., Enger, 1998] while others are using radiative boundary conditions [e.g., Orlanski, 1976]. In the present model, a so-called flow-relaxation zone, or sponge boundary condition, is used at the lateral boundaries [e.g., Davies, 1975]. The main idea is to add a relaxation term to the governing equations of any variable (Φ):

$$\frac{\partial \Phi}{\partial t} = \cdots - r(\Phi - \Phi_0) \tag{2.7}$$

where r is called the relaxation coefficient and Φ_0 the externally desired value of Φ at the boundary (it can be estimated from large-scale models), $r = r(x, y) \geq 0$, continuous and non-zero only in the vicinity of the boundary and reaching a maximum at the boundary. The region, where r is non-zero is called the flow relaxation zone. This increased filtering cannot be applied abruptly near the edge of the domain, as Morse (1973) pointed out, because it would cause reflections, analogous to those in optics when light crosses an interface of materials of different indices of refraction. A disadvantage of this technique is that we have to add some extra gridpoints to the model domain which contribute to the computational costs of our model.

At the top boundary, vertically propagating internal gravity waves can be reflected downward [Klemp and Lilly, 1975]. To overcome these problems the top of the domain should be removed as far as possible from the disturbance, up to the upper portion of the troposphere, and a so-called sponge-layer is introduced at the top boundary. This sponge layer is an artificially enlarged diffusion coefficient at gridpoints inside this layer. This can dampen waves and therefore reflection is reduced. On Figures 2.2 and 2.3 the variation of the exchange coefficient with height is plotted to demonstrate this sponge layer. Note that these arbitrary boundary conditions are nor physically nei-

[5]Local boundary condition which is generated at the boundary and is not a function of interior gridpoints

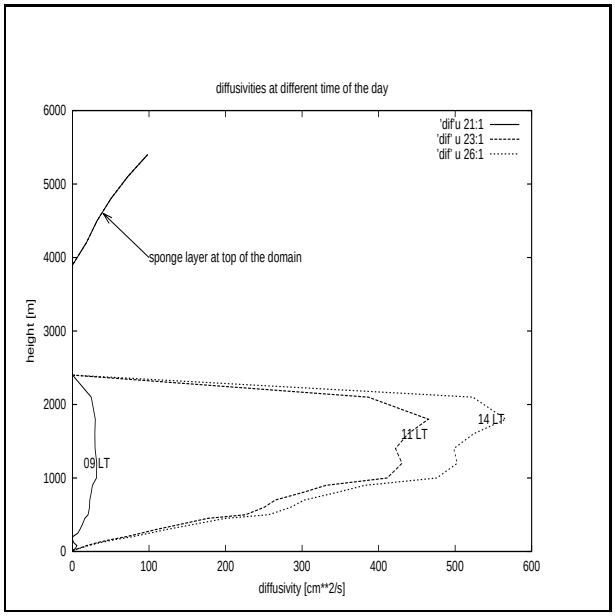

Figure 2.2: **Turbulent exchange coefficient**

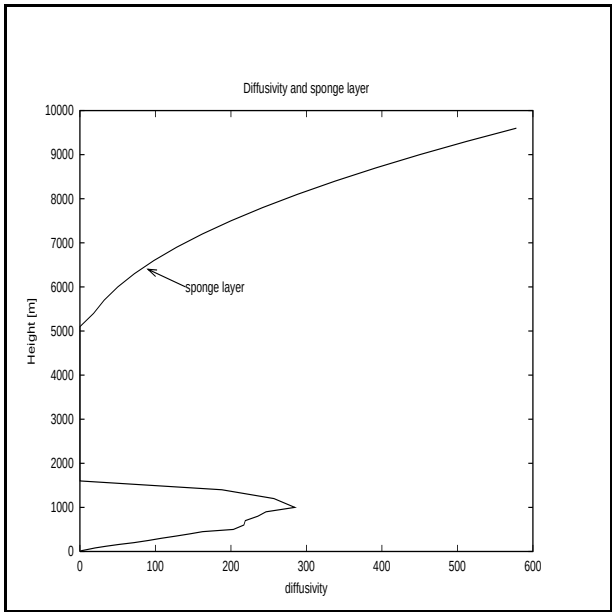

Figure 2.3: **Turbulent exchange coefficient**

ther mathematically adequate! Application of such technical methods is required for the sake of numerical stability. Introducing adequate boundary conditions which are mathematically correct may depend on future works.

2.3 Parameterizations

The lower boundary is the most important one. Only that has physical meaning and the major part of the mesoscale circulations are forced by surface inhomogeneities.

At the surface, the heat balance equation is considered:

$$Q_s + LE = R_n + L{\downarrow}n - \sigma T_s^4 - G \tag{2.8}$$

Here Q_s is surface heat flux, L is the latent heat of evaporation (2400 kJ/kg) and E is water vapor flux, R_n is net radiation, $L_{\downarrow}$ is the long wave radiation of the atmosphere, σ is Stefan-Boltzman coefficient, T_s is ground surface temperature (skin temperature) and G is heat flux down into or from soil layer. Parameterizations for each term:

The net insolation is obtained by Kondo's formula [J. Kondo, 1967]:

$$R_n = (1-\alpha)C_1 I_0 \cos Z(0.57 - 0.016e_m$$

$$-0.06\log_{10} e_m + (0.43 + 0.016e_m)10^{-0.13/\cos Z})$$

Here, C_1 is a factor of sunshine ($C_1 = 1$ for cloudless conditions, else $C_1 = 0.7t + 0.3$ where t is duration of sunshine), α is surface albedo, I_0 is the solar constant ($I_0 = 1370\ W/m^2$), e_m is vapor pressure near the surface in mbar and Z is the solar zenith angle:

$$\cos Z = \sin\phi \sin\delta + \cos\phi \cos\delta \cos\chi$$

where ϕ is latitude δ is solar declination and χ is the hour angle ($\chi = 0$ at 12 LST).

Long wave radiation of the atmosphere is obtained by the following equation [J. Kondo, 1967]:

$$L_{\downarrow} = \sigma T_m^4 (1 - (0.49 - 0.66\sqrt{e_m})(1 - C_2))$$

where T_m is air temperature near surface, C_2 is another parameter for cloud effect ($C_2 = n(0.75 - 0.005e_m)$, where n is cloud amount).

Heat flux from or into the ground is written as:

$$G = -c_g \varrho_g K_g \frac{\partial T_g}{\partial z}$$

where T_g is temperature, c_g is heat capacity, ϱ_g is density and K_g is thermal diffusivity of the soil.

In the soil layer the thermal conduction equation is solved:

$$\frac{\partial T_g}{\partial t} = K_g \frac{\partial^2 T_g}{\partial^2 z^2} \tag{2.9}$$

The ground heat flux is calculated with the the profile, obtained by Eqn 2.9.

The surface fluxes are calculated with the Monin-Obukhov Similarity Theory [Monin and Obukhov, 1954]. The profiles in the surface layer are assumed to be logarithmic:

$$\frac{\partial u}{\partial z} = \frac{u_\star}{\kappa z}\varphi_M(\xi) \tag{2.10}$$

$$\frac{\partial \theta}{\partial z} = -\frac{Q_s}{c_p \varrho_\star \kappa z}\varphi_H(\xi) \tag{2.11}$$

where $u_\star$ is friction velocity, Q_s is heat flux, κ is the von-Kármán constant, $\xi = \frac{z}{L}$ and L is the Monin-Obukhov length scale:

$$L = -\frac{c_p \varrho u_\star^3 T}{\kappa g Q_s}$$

Here T is averaged absolute temperature in the surface layer. The profile functions $(\varphi_M(\xi), \varphi_H(\xi))$ are obtained by J. Kondo (1975):

$$\begin{aligned} \varphi_M(\xi) &= (1-16\xi)^{-1/4} \quad \text{for } \xi < 0 \\ \varphi_H(\xi) &= (1-16\xi)^{-1/2} \quad \text{for } \xi < 0 \end{aligned}$$

$$\begin{aligned} \varphi_M(\xi) = \varphi_H(\xi) &= 1+6\xi \quad \text{for } \xi \le 0.3 \\ &= (1+22.8\xi)^{1/2} \quad \text{for } \xi > 0.3 \end{aligned}$$

Substituting these expressions into Eqn 2.10 and Eqn 2.11 and integrating the result from z_0 to the top of the surface layer, $h \cong 20\ m$ (to the lowest gridpoint of the model), gives expressions for Q_s and $u_\star$.

The vapor flux E for the estimation of the latent heat flux is parameterized as follows:

$$E = \beta \varrho \kappa u_\star \frac{q_0 - q}{\Psi_q} \tag{2.12}$$

where evaporation efficiency β is obtained by the canopy conductance method:

$$\beta = \frac{G_s}{\kappa u_\star + G_s}$$

where the canopy conductance G_s is an external parameter. The stability function for vapor Ψ_q is assumed to be equal to that for heat

$$\Psi_q = \Psi_H = \int_{z_0}^{h} \frac{\varphi_H(\xi)}{z}\, dz$$

and specific humidity of air at the surface, or more precisely at the z_0 level ($q_0 = q(z = z_0)$, is written as:

$$q_0 = \frac{6.22 e_s(T)}{p - 0.378 e_s}$$

assuming saturated air at the surface. Löwe's equation (which is a sixth order polynomial) is used to calculate vapor pressure:

$$e_s = a_1 T + a_2 T^2 + a_3 T^3 + a_4 T^4 + a_5 T^5 + a_6 T^6$$

Eqns 2.8-2.12 constitute the basic equations for the surface layer. These form a complete set in the dependent variables T_s, $u_\star$, Q_s and E. The equation system is solved by a kind of Newton-Raphson method. The first-guess values are assumed for the neutral case and iteration is executed 6 times.

Note that in this model phase change is considered only at the surface layer, otherwise water vapor is dealt as a passive scalar quantity, i.e., only advection and turbulent transport terms are assumed in the calculation, and source/sink terms (e.g./ condensation) are neglected. This can result in false super-saturation conditions. Release of the latent heat of condensation need to be considered through the so-called moist adjustment method, for example.

In the calculation of the concentration of carbondioxide the contribution of surface vegetation is assumed to be the sum of the uptake by photosynthesis and the release by respiration processes. For the prognostic equation of CO_2 concentration the following parameterization is assumed to calculate CO_2 fluxes at surface:

$$E_{CO_2} = \frac{bR_n}{1 + aR_n} - R$$

where a and b are external characteristic parameters of surface vegetation. Respiration R is given by the following expression:

$$R = R_{10} Q^{\frac{t-10}{10}}$$

where $R_{10} = 0.102\ m^{-2}s^{-1}$, $Q = 2.5$ and t is air temperature in degrees centigrade.

If any information about the anthropogenic heat and CO_2 emission are available, contribution of these data are assumed at the surface. The emission of a large stack contributes to the concentration of the grid point closest to its effective stack height. At the calculation of the effective stack height, plume rise is considered through the concave equation, as follows: Let the height of the stack be h, the amount of the discharged gas be X $[m^3 h^{-1}]$ and the temperature of it be T_e [Kelvin]. Air temperature $T(h)$ and wind $(u(h), v(h))$ are obtained at the height of the stack with linear interpolation between the two

closest gridpoints vertically. The concave equation for the plume rise is:

$$\Delta h = 0.175 \frac{\sqrt{c_p \varrho X \Delta t}}{|v|^{3/2}}$$

where:

$$|v| = \begin{cases} \sqrt{u^2+v^2} & \text{if this is larger than 0.4} \\ 0.4 & \text{else} \end{cases}$$

and

$$\Delta t = T_e - T(h)$$

The emitted gas is considered at the gridpoint which corresponds to the height $h + \Delta h$.

2.4 Closure

The vertical diffusion is parameterized using K-theory, a first order closure. Values of $K_V^{u,v}$ and K_V^{θ} in Eqn 2.2,2.3,2.5 are obtained as a function of the flux Richardson number (R_f)

$$K_V^{u,v} = l^2 |\frac{\partial u}{\partial z}| \frac{S_M^{3/2}}{\sqrt{c}} S_H (1 - R_f)^{1/2}$$

$$K_V^{\theta} = l^2 |\frac{\partial u}{\partial z}| \frac{S_M}{\sqrt{c}} S_H (1 - R_f)^{1/2}$$

when $R_f < R_{fc}$ and

$$K_V^{\theta} = K_V^{u,v} = 1.0\,[m^2 s^{-1}]$$

otherwise. The stability functions are:

$$S_M = \frac{1-C_2}{CC_1^2} \frac{HB}{G} \frac{R_{f1}-R_f}{R_{f2}-R_f} \frac{Rf3-R_f}{1-R_f}$$

$$S_H = \frac{B}{CC_1C_{1T}} \frac{R_{f1}-R_f}{1-R_f}$$

$$l = \frac{kz}{1+\frac{kz}{l_0}} \quad \text{[Blackadar(1962)]}$$

Here the following values were used for the symbols above: $R_{f1} = R_{fc} = 0.29$, $R_{f2} = 0.33$, $R_{f3} = 0.45$, $C_1 = 1.5$, $C_2 = 0.65$, $G = 2.32$, $C_{1T} = 3.2$, $B = 2.67$, $H = 1.7$, $C = 0.203$ and $l_0 = 100$ m. Basically this is a level 2 closure [Mellor and Yamada, 1974] with some correction by adding the effect of buoyancy [Gambo, 1978]. The bulk Richardson number Ri is calculated directly from the model variables, and flux Richardson number R_f is derived as follows:

$$Ri = \frac{K_V^{u,v}}{K_V^{\theta}} R_f \qquad (2.13)$$

from the expression for $K_V^{u,v}$ K_V^{θ} above:

$$\frac{K_V^{u,v}}{K_V^{\theta}} = \frac{S_M}{S_H}$$

Substituting into 2.13 gives the next quadratic expression for R_f as a function of Ri:

$$R_f = 0.91(0.248 + Ri - \sqrt{Ri^2 - 0.23Ri + 0.62})$$

Note that the vertical diffusion coefficient is a function of the Richardson number, which is function of the temperature gradient, therefore the diffusion coefficient has a daily variation, on Figure 2.2 the vertical profiles of the diffusion coefficient is plotted at different times of the day.

Diffusion in the horizontal direction is assumed to suppress numerical instability and has no physical meaning. The values for the horizontal diffusion coefficients were fixed by trial and error. Radiative transfer that works to back the temperature profile to initial lapse rate, is assumed. A Newtonian type cooling is introduced with a relaxation time (τ) of 3 hours. This process is important, in particular, for cooling in a basin [Kondo, 1986] stable layer formulation [J. Kondo, 1976] and for cooling of the atmosphere which was heated by sensible heat transfer from the surface in the daytime. When large scale data are also given as boundary conditions for the calculation, Newtonian cooling is assumed to work back the temperature profile to the interpolated large-scale gridpoint value, with the same relaxation time:

$$\theta = \theta - \frac{\Delta t}{\tau}(\theta - Bt)$$

where Bt is the original temperature profile. Formally, this means that a nudging term is added to the governing equation:

$$\frac{\partial \theta}{\partial t} = \cdots - G_\theta(\theta_{Observation} - \theta) \qquad (2.14)$$

where the nudging coefficient is the inverse of the relaxation time ($G_\theta = \frac{1}{\tau}$). Wind components are treated in a similar way: replace u and v with θ in Eqn 2.14. This kind of dynamic initialization technique has been suggested by Hoke and Anthes (1976).

2.5 Numerical solution of the model equations

The model equations (Eqns A.4-A.8 in Appendix A.2) form a set of coupled partial differential equa-

tion, which cannot be solved analytically but have to be discretized and solved on a finite grid mesh. Some variables (e.g., u, v, θ, q) are predicted by prognostic equations, while others (e.g., $\dot{s}$, π) are obtained through diagnostic expressions. Some of the terms are dealt with separately (e.g., vertical diffusion), using the time-splitting (or Marchuk-) method.

2.5.1 The advection scheme

Discretization of the advection term is based on the method described by Arakawa (1972). The basic idea of the method is a staggered grid network for u, v and θ in the horizontal plane and for θ, π and $\dot{s}$ in the vertical direction (this is the so-called Arakawa-grid or C-grid). Variables for each gridpoints are obtained by linear interpolation. Then the Arakawa scheme is used, which conserve both quadratic quantities (i.e., kinetic energy and enstrophy) and therefore ensure that no systematic one-way energy cascade occurs [Arakawa, 1964]. Finite difference analogues of the advection terms in Eqn A.5, as an example to the Arakawa scheme are presented in Appendix B.1. The Leap-frog scheme is used for time integration of the advection term and a forward step is used every 20 steps to remove the computational mode and the large frequency noise caused by the departure of this computational mode from the physical mode (This large frequency noise appears even on the diagram of the model variables, as can be seen on Figure 2.4, for example).

2.5.2 Diffusion

In the horizontal diffusion terms of Eqns A.5-A.8 the terms $\frac{\partial}{\partial x}K\frac{\partial}{\partial x}$ and $\frac{\partial}{\partial y}K\frac{\partial}{\partial y}$ are much greater than the other terms, so the others were neglected. Horizontal diffusion is not considered for physical meaning, but so as to suppress numerical noises. Horizontal diffusion coefficients are obtained by the method of Takano (1976) with some simplifications. The expression for the horizontal exchange coefficients for any variable (Φ) is as follows:

$$K_H^{\Phi} = \Delta^2 C_4 |\Phi_{i+1,j,k} + \Phi_{i-1,j,k} + \Phi_{i,j+1,k} + \Phi_{i,j-1,k} - 4\Phi_{i,j,k}|$$

where $\Delta = \Delta x = \Delta y$, and $C_4 = 0.0002$ tentatively fixed by trial and error. If this expression gives $\frac{K_H^{\Phi}}{\Delta^2}$ smaller than 0.0001 or larger than 0.002, $\frac{K_H^{\Phi}}{\Delta^2}$ is put equal to these threshold values. In contrast to velocity, potential temperature can have large vertical variation, neglecting those terms containing the difference of the height of the iso-s surfaces (terms containing $\frac{\partial \log D}{\partial x}$) can lead to false diffusion of heat. The diffusion coefficient for heat is calculated in the same way as for momentum, but no minimum value is given. For the formula of each diffusion term see Appendix B.2

Time integration is performed by forward explicit scheme with a timestep of $2\Delta t$.

The diffusion term in the vertical direction is maintained implicitly to reduce it's computational cost. An explicit solution requires an extremely short timestep (i.e., $\Delta t \leq \frac{\Delta z^2}{2K_V^{\Phi}}$). An implicit trapezoidal method is used, instead. For a two dimensional array in the x–z plane Gaussian elimination is performed and the same timestep as for the advection term is assumed.

2.5.3 Pressure Gradient

The pressure gradient term in the momentum equation for u (Eqn A.5) is written as:

$$-\theta D\{\frac{\partial \pi}{\partial x} - (s-1)\frac{g\theta}{\Theta^2}\}$$

The vertical grid for π and Θ are staggered so the scheme for pressure gradient term of u has the form as written in Appendix B.3. Time integration for pressure gradient term is maintained in the same way as for the advection term, i.e., leap-frog scheme with the same timestep, and using a forward scheme every 20 steps.

2.5.4 The Coriolis term

On the C-grid u and v are staggered in the horizontal plane, so v for u gridpoints is calculated with the average of the 4 v gridpoints around u. This averaged value is used for the calculation of the Coriolis term:

$$\frac{1}{4}f(v_{i+\frac{1}{2},j} + v_{i-\frac{1}{2},j} + v_{i,j+\frac{1}{2}} + v_{i,j-\frac{1}{2}} - v_g)$$

Time integration is the same as for the pressure gradient term.

2.5.5 Hydrostatic Equation

The mesoscale scaled-pressure deviation (π) is obtained by the integration of a diagnostic equation derived from the hydrostatic equation (Eqn A.7). π

and θ have the same gridpoints on the iso-s projection, and are staggered vertically. In the execution of the integration, π is set equal to zero at the top boundary and integrated from top to bottom:

$$\pi_{i,j,k} = \pi_{i,j,k-1} - \frac{g\theta}{\Theta^2} D_{i,j} \Delta s_k$$

Note that the vertical index (k) increase from top to bottom, i.e., $k = 1$ at the top of boundary.

2.5.6 Continuity Equation

The non-dimensional vertical velocity ($\dot{s}$) is to be obtained by the integration of the continuity equation (Eqn A.4). The $\dot{s}$ and u, v planes are staggered vertically, and the projection of $\dot{s}$, u and v are staggered in the x and y directions, respectively. Thus the scheme for continuity equation should be written as:

$$F_{i+\frac{1}{2},j,k} - F_{i-\frac{1}{2},j,k} + G_{i,j+\frac{1}{2},k} - G_{i,j-\frac{1}{2},k}$$

$$+(S_{i,j,k+\frac{1}{2}} - S_{i,j,k-\frac{1}{2}})/\Delta s = 0$$

where

$$F_{i+\frac{1}{2},j,k} = \frac{1}{2}(D_{i+1,j,k} + D_{i,j}) u_{i+\frac{1}{2},j,k}$$

$$G_{i,j+\frac{1}{2},k} = \frac{1}{2}(D_{i,j+1,k} + D_{i,j}) u_{i,j+\frac{1}{2},k}$$

$$S_{i,j,k+\frac{1}{2}} = D_{i,j}) \dot{s}_{i,j,k+\frac{1}{2}}$$

At surface $\dot{s} = 0$ and integration is executed from bottom to top.

2.6 Initialization

On the mesoscale, adjustment is considered to the geostrophic wind, in contrast to pressure or geopotential height in synoptic-scale models. The model do not have a latitude–longitude projection, so Coriolis terms are non-separable, which makes normal mode initialization even more difficult. In addition, some important model variables are not initial parameters, but used in the calculation of the model variables (e.g., exchange coefficients, surface parameters, vertical velocity, etc.). Calculation should be started well before the period we are interested in (dynamical initialization). The spin-up time is the shortest time, if we start the integration at noon (12 LT). This spin-up time can be visualized on top panel of Fig 3.13: the initial kinetic energy decreases until the steady state, which corresponds

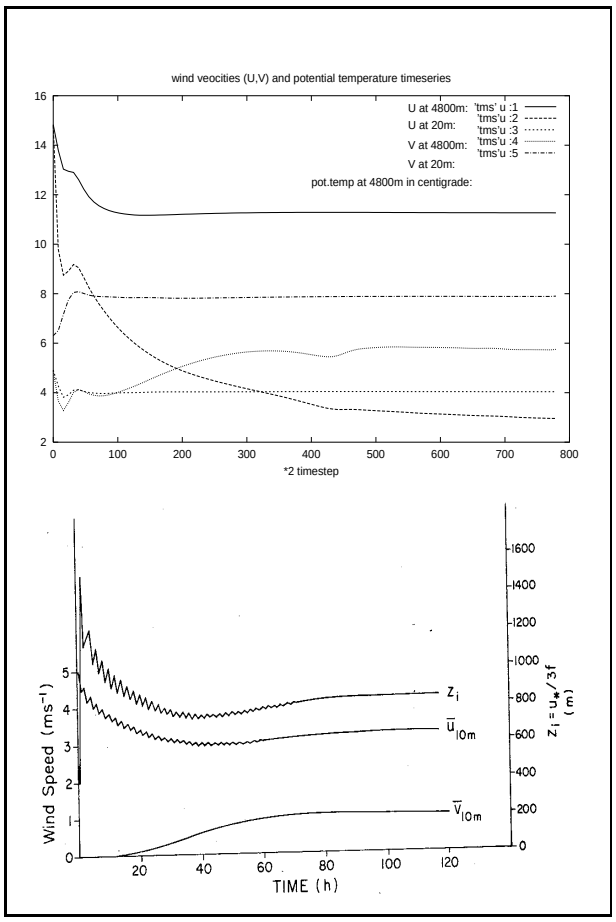

Figure 2.4: **Top: Time variation of the different variables. Bottom: Initialization in a mesoscale model [Kessler, 1982].**

to the mesoscale balance state. On top panel of Fig 2.4, which is an output from this model, we can see that the wind components are changing in time, until the steady state is generated. After 400-500 timesteps the order of their magnitude becomes constant.

Chapter 3

Adaptation of the NRIPR Model

Mesoscale meteorological numerical models cannot be used for different environments directly. Mesoscale phenomena are mainly topographically induced, or heterogeneities of the surface parameters are responsible for the circulations. If we simply change the model topography and landuse data fields, the model has to be tested before establishing the fidelity of the model simulations. After the proper data fields have been generated for the model, simulations should be performed for simple cases to evaluate the results.

So as to run the NRIPR mesoscale model with respect to only the meteorological variables, the following database is needed in the proper form:

1. Topography data, average elevation for each gridbox

2. Different land cover databases:

   - land-sea index: different calculation is performed over land and sea surfaces
   - area (m^2) for different categories of landuse in each gridbox for the calculation of surface heat balance
   - fraction of vegetation (%) in each gridbox

3. large-scale meteorological data, and initial data fields

3.1 The Topography Database

The first run was performed on a topography database, which was obtained from the Digital Telecommunication Map (DTM3000) dataset. This dataset was generated at the Experimental Institute of the Hungarian Post[1] in the late 1970's. The resolution of the original dataset is approximately 3 km in the x and y directions or more precisely, the longitudinal resolution is $\Delta\lambda = 150''$ and the latitudinal is $\Delta\varphi = 100''$. For each gridbox the maximum elevation, the deviation of the elevation, and some land cover information[2] are given, based on a NATO aeronautical chart (1:100000) from the 1960's. Surface informations have changed a lot since then, so another database is used for the present calculations. This latter database was generated from a portion of the EROS[3] global land cover and topography dataset, from a Lambert Azimuthal Equal Area map projection, which has a 1km nominal spatial resolution based on 1 km AVHRR[4] data. The use of this dataset is convenient, because land cover information with the same parameters (i.e., same projection, resolution and grid network) is available for the calculation. In addition, using an automatically generated database preclude the possibility of containing such errors, as can be contained in the first database, which was generated by human effort. This database can be obtained through anonymous file transfer protocol[5] in compressed binary files. Data of the considered area were taken from the file for Eurasia, optimized for Europe, transformed from Lambert Azimuthal Projection to Cartesian, and put into ascii files, suitable as input for our model. A chart showing the considered area in Lamberth projection is presented in the down left panel of Fig 3.1. The resolution and extension of the model domain can be chosen before each run.

[1] the forerunner of todays Hungarian Telecommunication Company (MATAV)
[2] with only 4 different categories
[3] Earth Resources Observation System
[4] Advanced Very High Resolution Radiometer
[5] edcftp.cr.usgs.gov

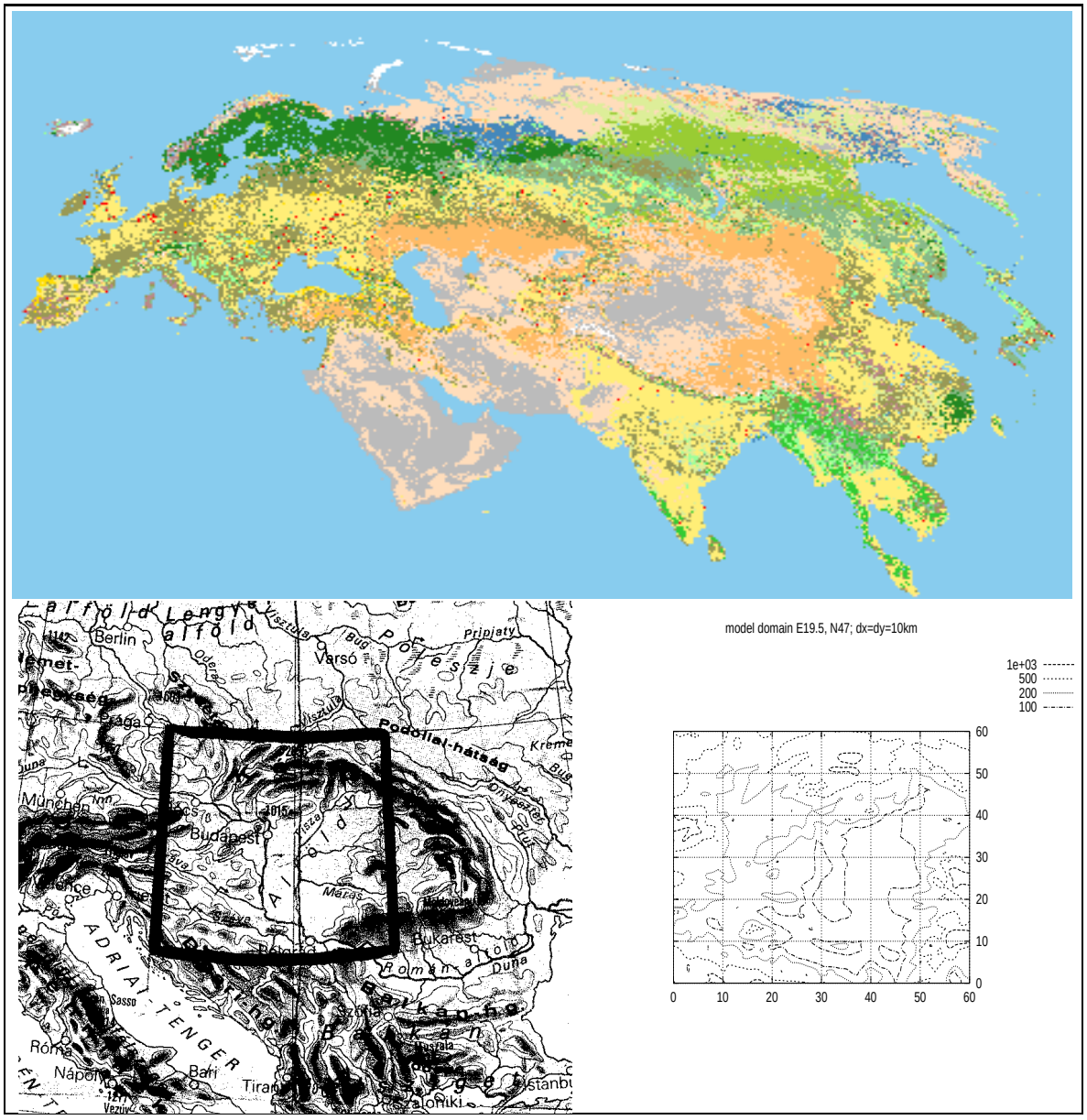

Figure 3.1: **The model domain. Top: Database of the Eurasian region in Lambert Azimuthal equal area projection. Bottom left: The considered area in Lambert projection. Bottom right: The model domain for the standard run in Cartesian system.**

However, the domain usually used in the standard run is one with a horizontal extension of 600 kms both in x and y directions, with a spatial resolution of 10 kms centered at E19.5^o N47^o, a location in the middle of the Carpathian basin (see Fig 3.1 down right). Representative elevation for each gridbox is simply calculated using arithmetic mean of the contributing data for that gridbox. Using for example an interpolation based on the weight inversely proportional to the distance from the gridpoint can result in larger deviation in altitude. Although the topography data field should be smooth enough, to avoid erroneous gravity waves, which can generated by the interaction between flow and topography.

3.2 Model Evaluation

Pielke (1984) pointed out six criteria for the evaluation of a mesoscale meteorological model. These requirements are:

1. The model must be compared with known analytic solutions
2. Non-linear simulations of the model should be compared with other models, which have been developed independently
3. The mass and energy budget must be computed to determine the conservation of these important physical quantities
4. The model predictions must be quantitatively compared with observations
5. The computer logic of the model must be available on request, so that the flow structure of the code can be examined
6. The published version of the model must have been subjected to peer review

As the writer of this paper has worked with the source code of the model, investigated and become familiar with the computer logic of the model, which satisfies criterion No.5. In these sections model results are compared with observation (criterion No.4.) or other model results (No.2.), if available. For some simulated events brief theoretical discussions are also included (criterion No.1).The energy budget has also been calculated, when seeking for any large frequency noises (No.3).

3.3 Dynamical Test

After obtaining the topography dataset, some runs were performed to test it's suitability. These runs were performed with arbitrary land cover data, i.e., the same type of land cover (grass) were considered for all gridpoints. Horizontal variation of surface parameters (surface temperature and fluxes) was eliminated, and only the effect of the interaction between the flow and topography was studied this way. Vertically 35 gridpoints were considered up to 5400 m height and a 1500 m thick sponge layer (uppermost 6 grids) was used. Initial conditions for the first three run were neutral stratification (with an initially constant 299 K potential temperature), light synoptic breeze $(u_g, v_g) = (0, 2)\ ms^{-1}$ with no vertical shear. All calculations were performed at 204 Julian day, i.e., 23 July. Time variations of the vertical profiles of temperature and wind were studied in one gridpoint in the center of domain. The terrain of this site is relatively flat, free from large deviation in the altitude within 50 km radius (see Fig 3.1). The energy budget in the model calculation (Fig 3.3) was was compared to measurements [e.g., Oke, 1987](Fig 3.2). According to the diurnal cycle of surface heating, air temperature within the lower layers has a daily variation, too. Time variation of the lower 800 m temperature and some

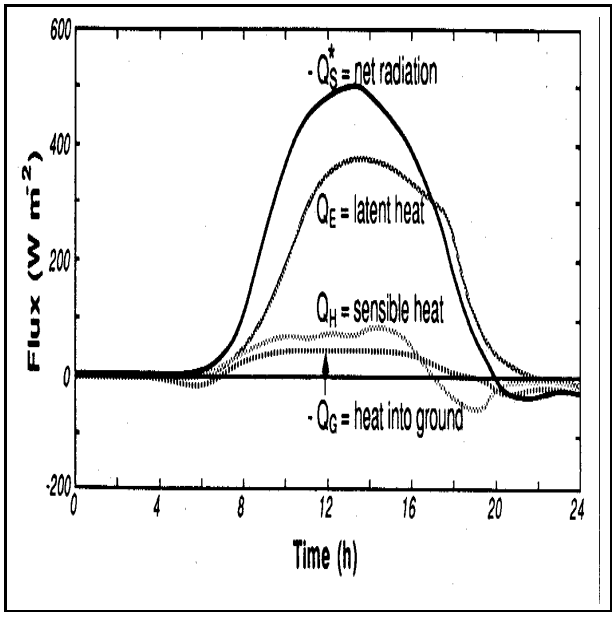

Figure 3.2: **Measured energy balance components [Oke, 1978]**

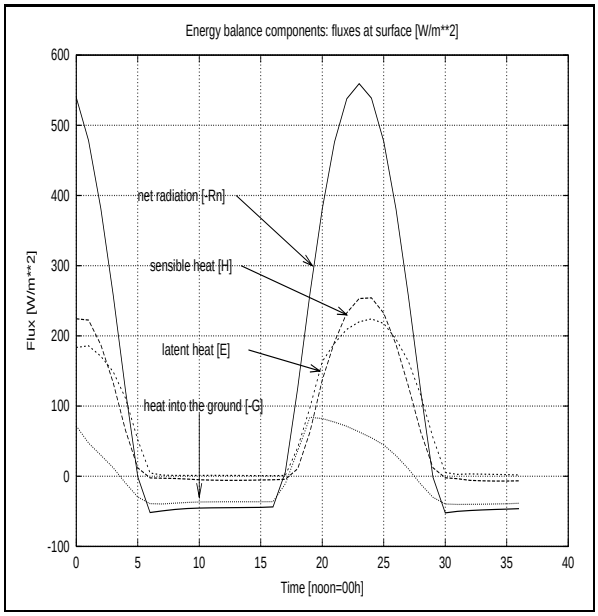

Figure 3.3: **Time variation of energy balance components in the calculation.**

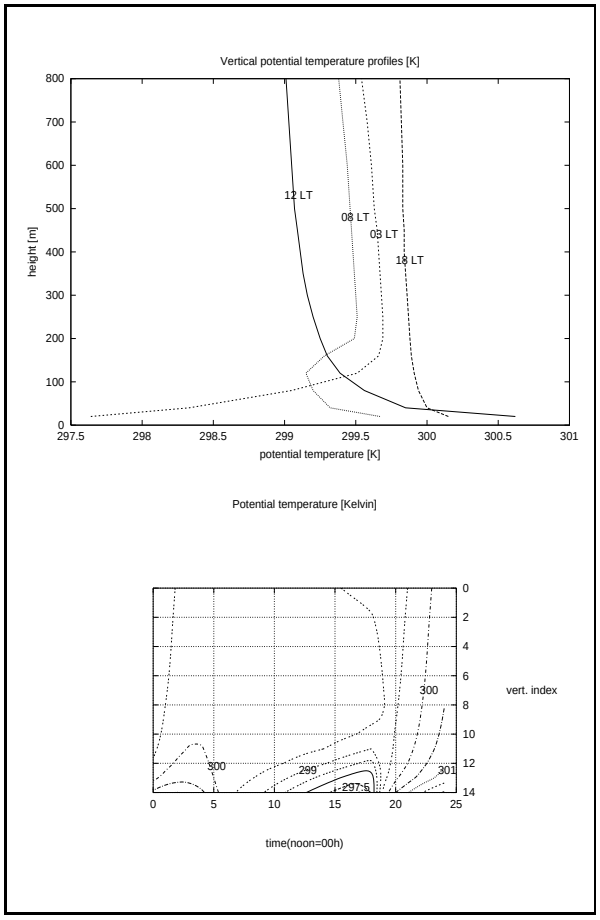

Figure 3.4: **Time and space variation of potential temperature**

significant temperature profiles are shown on Fig 3.4. As we can see, a fairly unstable surface layer during the day and a slightly stable layer developing at night, due to heating or cooling of the lower layers by surface. This generates intensive vertical turbulent exchange at daytime, while in stable case vertical exchange is negligible (see Fig 2.2). Vertical variation of the wind velocity components show a veering of the Ekmann type: the wind direction changes counterclockwise at lower levels (Fig 3.5) In addition, wind speed increases and become super-geostrophic during the nighttime stable conditions. This feature can be characterized as a Low-Level Jet (LLJ) event, if we define LLJ as a vertically thin, horizontally extensive layer of air, traveling at a super-geostrophic speed, causing a wind maxima within the lower layer, i.e., below 1500 m [e.g., Bonner, 1968]. LLJs occur as a result of a variety of forcings. Among them are synoptic-scale baroclinicity, fronts, baroclinicity due to sloping terrain, advective accelerations, confluence and ducting around mountain barriers, land and sea breezes, mountain and valley wind and inertial oscillations [Stull, 1988]. A stable stratification is generally needed for LLJ, otherwise vertical mixing tends to eliminate wind maxima. In the present calculation at this location an inertial oscillation could cause super-geostrophic wind speed during stable conditions. As it will be shown below, an inertial oscillation is a possible analytical solution for the governing equations of the model (in the absence of frictional forces, an assumption that can be made only with a stable stratification).

Let us consider the model equations for the horizontal wind velocity components u, v in the Cartesian system (Eqn 2.2-2.3) using the Lagrangian time derivative notation, neglecting the mesoscale pressure gradient terms, and using the notation $V^\star = (u_g - u) - i(v_g - v)$, where $i = \sqrt{-1}$. $V^\star$ expresses the geostrophic departure vector on the complex plane. The calculations were performed at constant geostrophical forcing, $u_g = v_g =$ constant in time. At night turbulent exchange coefficients are negligible, so vertical momentum flux vanishes. The horizontal momentum equations can be written

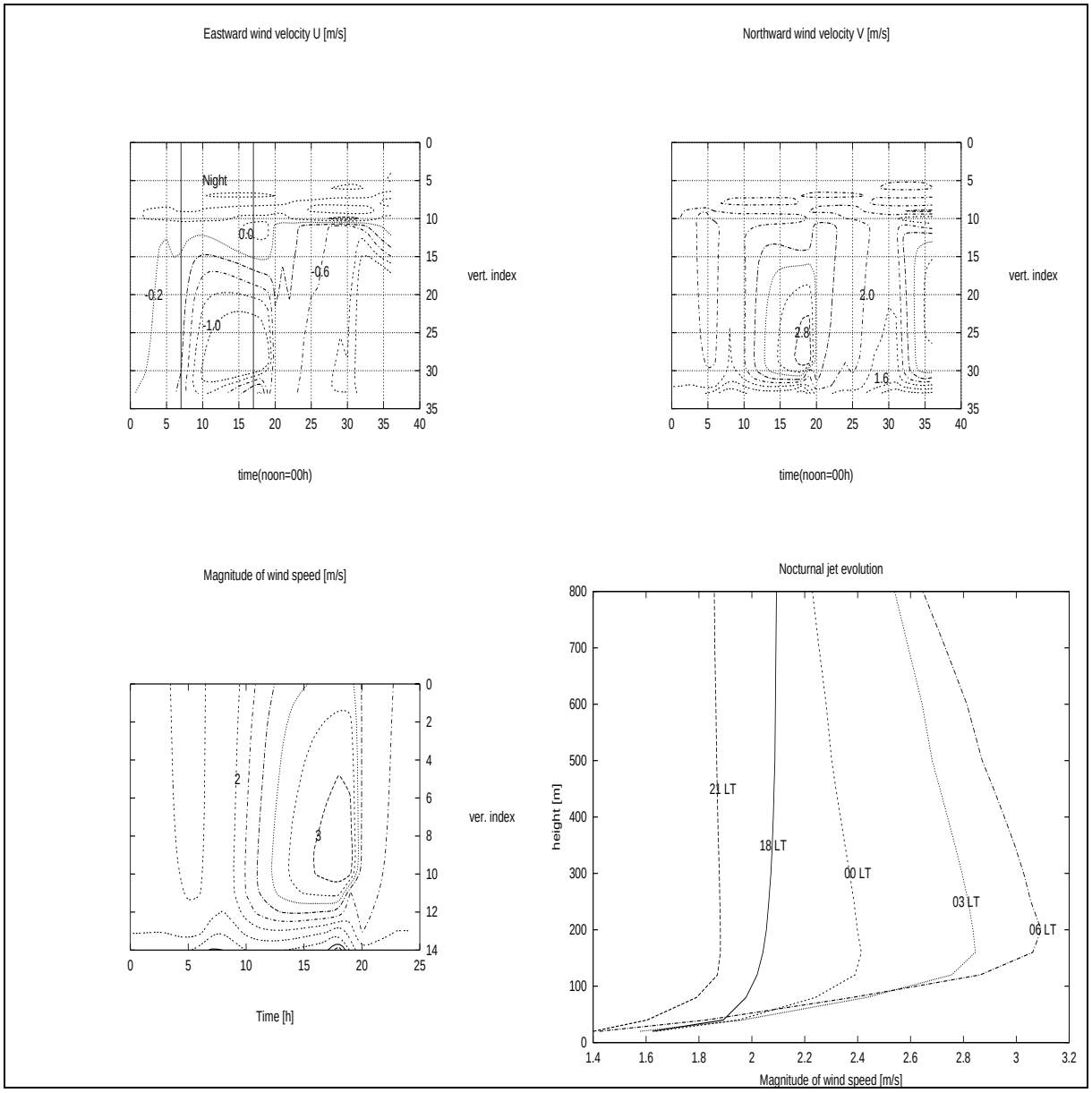

Figure 3.5: **Time and space variation of wind. Top: Time variation of vertical cross-sections of u (left) and v (right) wind velocity components. Bottom: The same for the wind speed (left) and profiles of wind speed at different times of the day.**

in complex form:

$$\frac{dV^\star}{dt} = -ifV^\star$$

This has the solution:

$$V^\star = V_0 e^{-ift}$$

where V_0 is to be determined from the initial conditions (complex geostrophic departure at sunset). This is the equation of a two dimensional harmonic oscillator, with a period of $\frac{2\pi}{f} \cong 14$ hours at midlatitudes. The wind vector will follow a Lissajous curve in the (U, V) phase space (Fig 3.6). Essentially, the

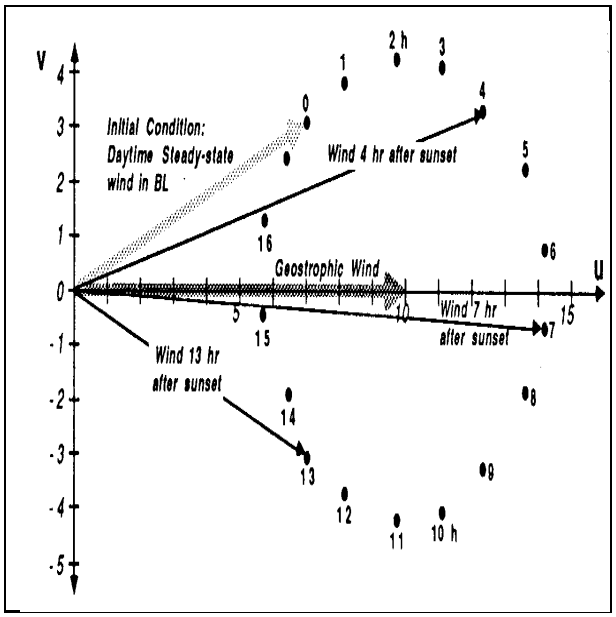

Figure 3.6: **Inertial oscillation of the wind [Taken from Stull, 1988]**

nocturnal stable layer is non-turbulent, decoupling the air above from significant frictional surface influences. Thus the pressure gradient and Coriolis forces are left in an attempt to balance one another, with the initial perturbation being the removal of frictional forces. The Coriolis force accelerates the air unhindered by frictional forces. The adjustment overshoots, and an undamped oscillation develops. As mid-latitude nights last between 8 to 16 hours, the inertial oscillation may not even complete one period before daytime mixing destroys it. As it can be seen on Fig 3.5, shortly after sunrise (17th hour of calculation), the low-level wind maxima disappears.

Since the model was tested successfully at NIRE [Kondo, 1989] and for light synoptic breezes seemed to provide reliable results, a dynamical test for strong synoptic-scale wind was performed. Initial conditions for this run were strong geostrophic wind ($(u_g, v_g) = (1, 10)\ ms^{-1}$ with a vertical shear from ground up to 1000m: $\partial_z u_g = 0.001\ s^{-1}$, $\partial_z v_g = 0.008\ s^{-1}$). Temperature stratification was still assumed to be statically neutral. The time step for the numerical integration, as in the previous runs, was $\Delta t = 30\ s$. In the 40th step numerical instability occurred. A snapshot in two horizontal cross-sections (20m and 4000m above terrain) show the typical state of the model variables after 38 steps of integration on (top panel of Fig 3.7). At the 41st timestep Not A Number (nan) values appeared in the array of the prognostic variables. Such numerical instability can be caused by a variety of reasons. As the instability occurred during a run performed for an initially strong synoptic wind, an obvious reason for it could be the failure of the Courant-Friedrichs-Levi (CFL) stability criterion. The CFL for the linear advection term is:

$$C := \frac{u_0 \Delta t}{\Delta x} \leq 1 \tag{3.1}$$

where u_0 is the magnitude of the linear advection velocity[6]. For non-constant advection velocities, a local Courant number can be approximated by using the supremum of the wind speed as an estimate of u_0. Although the advection velocity was larger in this run than in the previous one, the grid interval is $10000m$, and the timestep is $30\ s$, which give a Courant number on the order of 10^{-2}. It is obvious that this instability was caused by another reason. The stability parameter of the parabolic term (diffusion) is the Fourier number, which is inversely proportional to the square of the grid interval in an explicit scheme. Vertical diffusion is dealt implicitly which is unconditionally stable, for the horizontal diffusion coefficient a maximum value was given, which still gives a Fourier number less than unity (Section 2.5.2). Another run with the same conditions but using a much shorter timestep ($\Delta t = 3s$) performed stable and realistic solution even after 1200 timesteps (Fig 3.7 bottom). This fact obviously shows that a disturbance, propagating much faster than the advection velocity caused numerical instability.

[6] C is often referred to as the Courant number

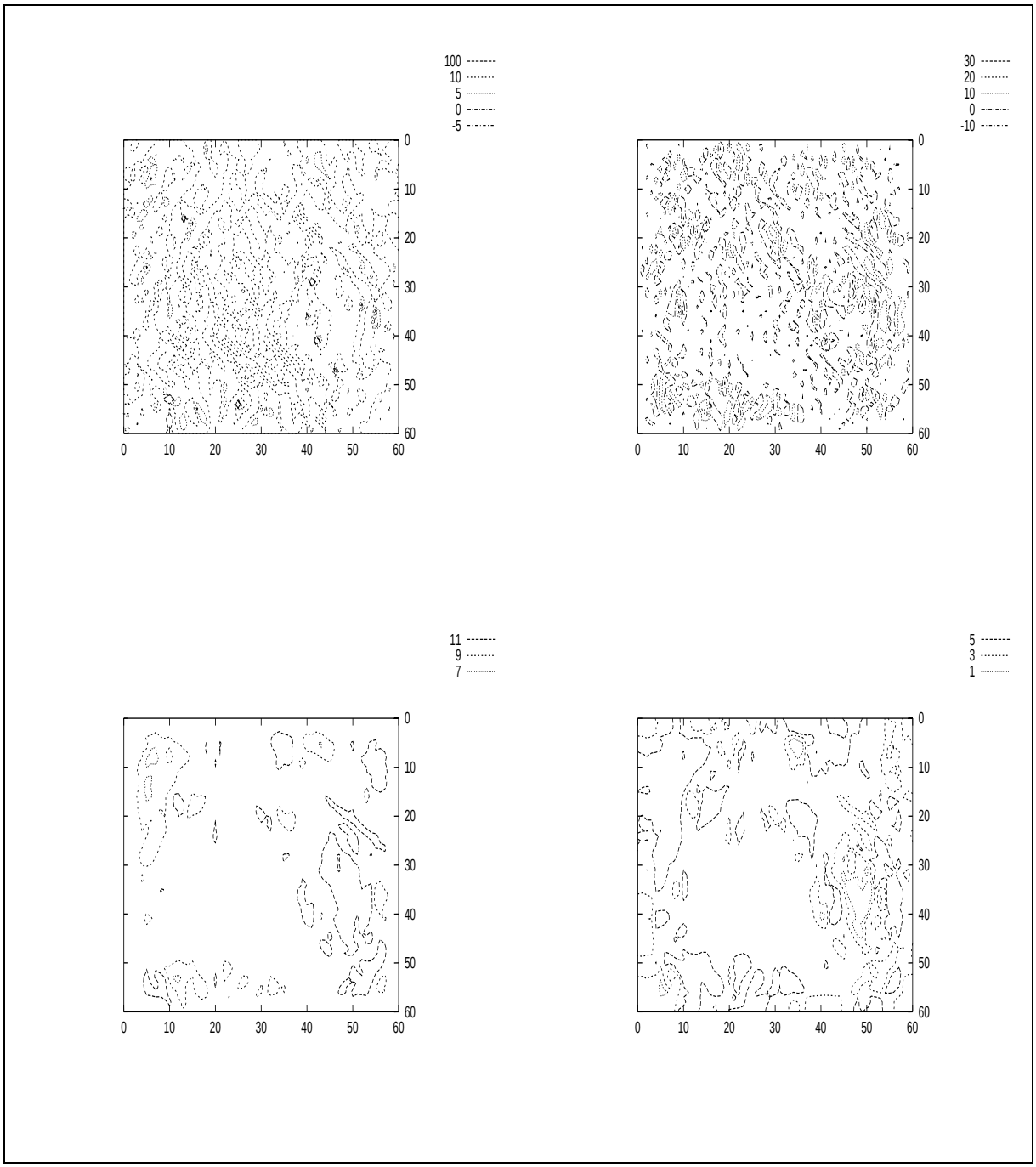

Figure 3.7: v **wind component at 4000m (left) and 20 m (right) above the surface, using timestep of 30 s (top) and 3 s (bottom)**

For example, in a much more simple case, when adjustment is considered through the shallow water equation [Tank Model, e.g., Pielke, 1984], the only other term is a linear advection term and a leap-frog in time central in space scheme is used. This gives the next CFL stability criterion:

$$C := \frac{(u_0 + \sqrt{gH})\Delta t}{\Delta x} \leq 1$$

As we can see, the phase speed of the shallow water waves contributes to the speed considered, and this gives a much stronger criterion than Eqn 3.1 for the time step in a still linear system. Note that this criterion is mainly determined by the gravity wave speed. It is essential then to remove these gravity waves from our model. For a primitive equation model the stability criterion of the complete set of equations is much more complicated.

There are three main sources of gravity waves in a primitive model:

1. Initial unbalance: if the initial conditions are unbalanced, adjustment of the model can generate gravity waves. It is well known that geostrophic initial conditions are not adequate for a mesoscale model [Daley, 1991]
2. Physical parameterizations (e.g., convection)
3. Topography

Topography can generate a number of different kinds of gravity waves (some examples are shown on Fig 3.8 Top). Moreover if the Froude number of the flow passing topography is becoming supercritical over the obstacle, an extremely large gradient can occur at the surrounding area. This results in a Hydraulic Jump under special conditions (Fig 3.8 bottom).

If such horizontally and/or vertically propagating large frequency waves once generated in the model, they might be reflected and amplified by non-adequate lateral and/or top boundaries, respectively. In addition the model boundaries can not only reflect, but even generate large frequency waves, as mentioned in Section 2.2. The stability criterion for such waves requires an extremely short time step. It's computational cost would be enormous, so it is necessary to remove these gravity waves. To localize the trigger effect, several runs were performed for the same initial conditions but for arbitrary boundary conditions:

1. Run without topography to test the effect of the physical parameterizations

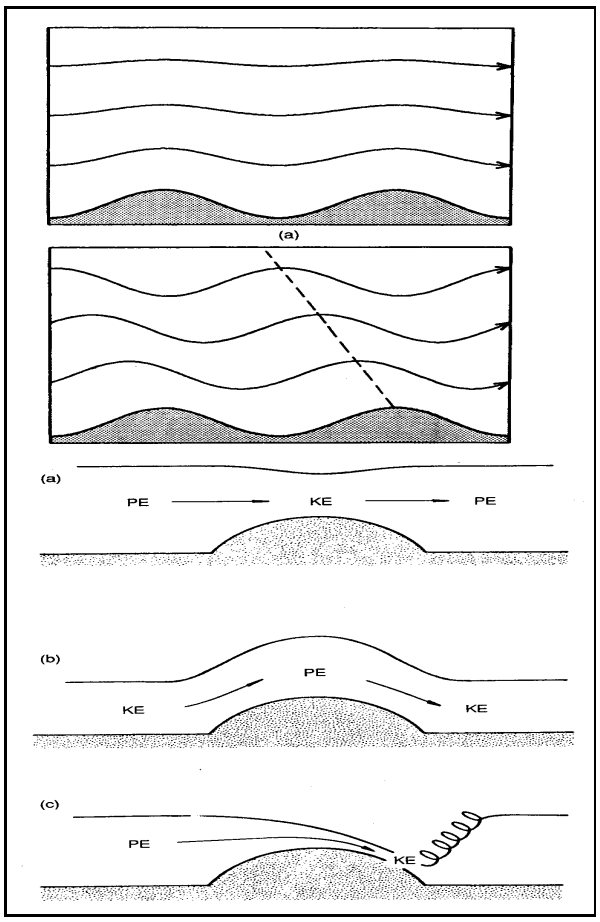

Figure 3.8: **Top: Different gravity waves generated by the topography Bottom: Flow around an obstacle for different Froude numbers, Hydraulic Jump**

2. Run without parameterizations to test the effect of topography
3. Run without either topography or parameterizations to test the dynamics of the model

Figure 3.9 shows contour isolines of u wind velocity component in a zonal cross-section of the model domain (in the x–z plane) at the end of the first hour of calculation of a 1. type run. This is an obvious evidence in support the fact that large frequency gravity waves were generated at the lateral boundaries and travelled with a phase speed on the order of 40 ms^{-1} into the interior of the domain. They were superimposed on each order, and reflected back from the boundaries. This effect was systematic and undamped, and so produced a fatal rise in the wave energy. Numerical experiments

proved that this process developed approximately 5 times faster when topography was also included in the model run.

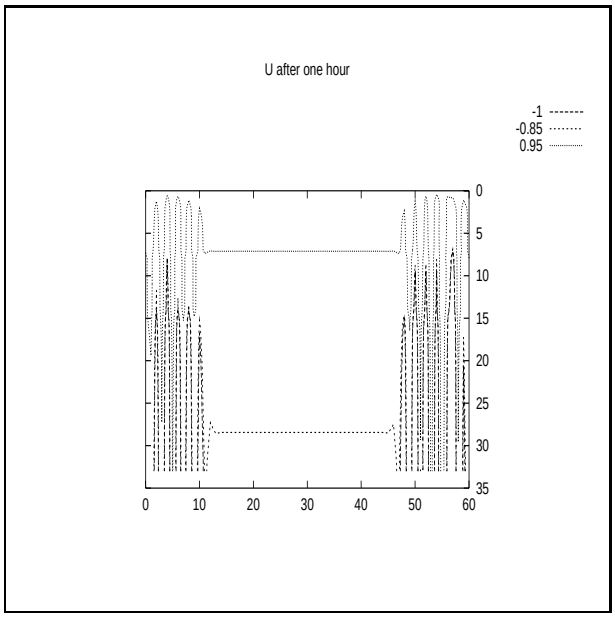

Figure 3.9: **Gravity waves generated by the lateral boundaries**

The instability[7] arose at the 41st timestep in a run, when the real topography was assumed (Fig 3.10 top). To test the sensitivity of the boundaries for topography, the terrain near boundaries was set equal to zero (i.e., flat terrain) for two gridpoints near the lateral boundaries (Fig 3.10 middle):

$$\frac{\partial z_G}{\partial x} = \frac{\partial z_G}{\partial y} = 0$$

Instability occurred only after 280 steps compared to 38, when topography was not smooth, which shows how sensitive the model is to boundary conditions. In the dynamical run (i.e., no topography or parameterizations), instability occurred after 850 timesteps.

The above facts show that the boundary conditions were not adequate for such initial conditions. These tests supported the fact that limited area models are usually very sensitive for the lateral boundary conditions. In addition, the model boundary coincides with the largest deviation in the topography. As further numerical experiments showed, some vertically propagating waves were reflected from the top boundary, too. As already mentioned in Section 2.2, this top boundary should be removed as far, as it's possible from the disturbances.

[7] Instability here is referred to as the first occurrence of the nan values

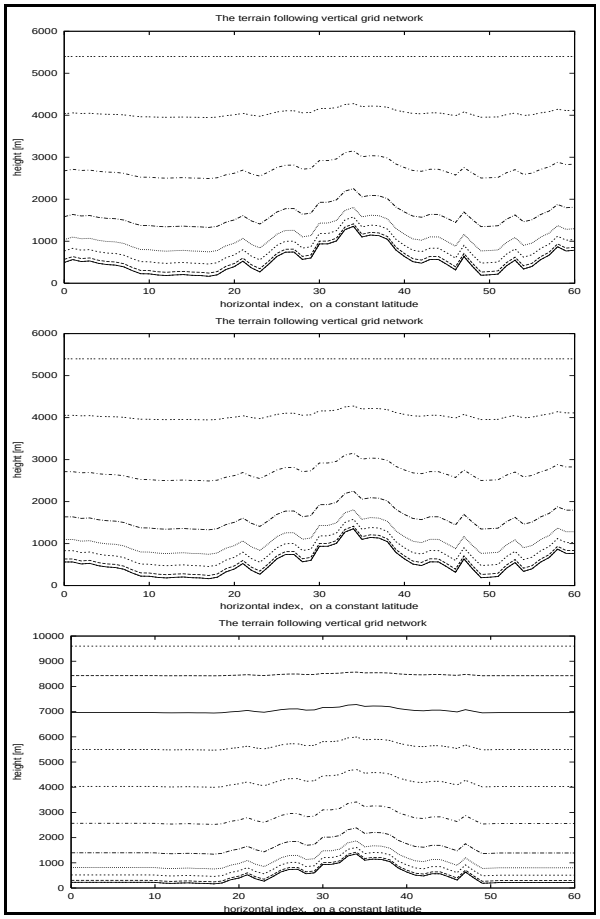

Figure 3.10: **Topography cross-sections**

It is easy to show that viscosity can dampen short waves for a Fourier number $\geq 1/4$, while it won't affect the long waves. Therefore, viscosity can be a powerful tool in damping large frequency noises. On the other hand, assuming too large a viscosity can cause unrealistic damping, and therefore an artificially loss of model energy.

To overcome numerical instability and remove gravity waves, the following steps were taken:

1. A flow relaxation zone for 10 gridpoints at each boundary is to be considered (see Eqn 2.7 in Section 2.2 for the scheme), where the relaxation coefficient r is expressed as a function of distance from the lateral boundary:

$$r = \frac{K}{i}$$

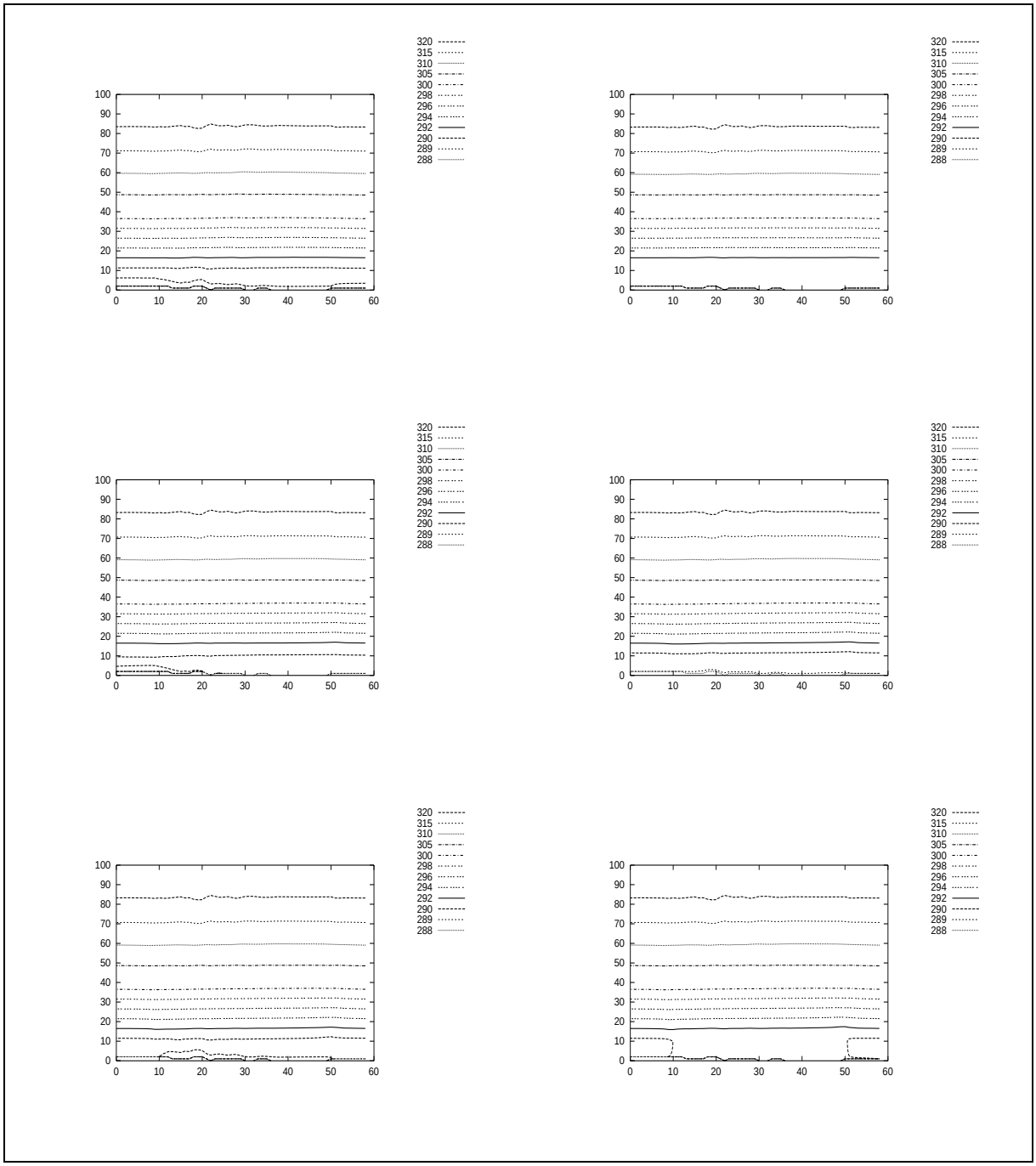

Figure 3.11: **East–west cross-sections of temperature at 13, 15, 19, 5, 10 and 12 hours, respectively.**

where i is the distance from the lateral boundary and K is tentatively put equal to 0.5.

2. The model topography was smoothed in the flow relaxation zone [i.e., elevation of the ground in the flow relaxation zone is equal to the elevation of the ground at the inner boundary of the flow relaxation zone (see Fig 3.10 bottom)]

3. Vertically 49 gridpoints were assumed up to 9600 m, instead of 35 gridpoints up to 5400 m. (Note that on the bottom figure of 3.10 the model domain is vertically more extensive)

4. A deeper and stronger sponge layer was prescribed for the top boundary (16 vertical grid, from 5100 m up to 9600, instead of 3900–5400 m, compare Fig 2.2 top and bottom)

This version of the model was tested for different initial conditions.The model performed stable run even in case of strong synoptic wind ($> 20ms^{-1}$!). Different vertical cross-sections in meridional and zonal directions were plotted to study the behavior of large frequency gravity waves. Horizontal cross-sections were plotted at different levels, so that the spatial variation of each variable within the whole model domain can be visualized at different timesteps. These figures and diagrams visually proved that the above listed techniques overcome the amplification of the wave energy. The inner domain of the model was free from large frequency waves, though some wave-like structure usually occur at the inner boundary of the relaxation zone. These disturbances could not escape from here, and no reflection occurred into the considered area. Moreover, these steady waves usually became weaker during the run. If some initial noises had appeared in the fields of variables at the end of the first hour, such noises "died-out" during the model run. For example, Fig 3.11 shows zonal cross-sections in the middle of the model domain during run with strong synoptic-scale wind at different times of the day. The initial potential temperature lapse rate was neutral up to 1000 m (i.e., $\frac{\partial\theta}{\partial z} = 0$), and slightly stable ($\frac{\partial\theta}{\partial z} = 4\ \frac{K}{km}$) above. It can be seen on these diagrams that there is a sharp contrast near the relaxation zone. This contrast more emphatic in the fields of velocities especially in the case of light geostrophic wind. This shows that the sponge boundary condition was applied abruptly, which can bias the model results, as quoted Morse in Section 2.2. The spectral HIRLAM uses a cosine-shape boundary relaxation factor [Gustafsson *et al.*, 1988] and the MIUU uses one inversely proportional to the square of the distance from the boundary [Enger, personal communication]. To dampen this sharp contrast, the expression for the relaxation coefficient r was changed to a sinusoidal function. In addition, the K coefficient also depends on the magnitude of wind speed (adaptive relaxation):

$$r = \frac{K}{5(1 - \cos(\frac{i\pi}{10}))}$$

where i is the horizontal index from the lateral boundary and

$$K = \begin{cases} 0.3 & \text{if } |\mathbf{v}| \leq 5\ ms^{-1} \\ 0.5 & \text{otherwise} \end{cases}$$

Recently, a relaxation factor inversely proportional to the square of the distance from the lateral boundary was used. It yielded the best results:

$$r = \frac{K}{i^2}$$

For the comparison of the linear sin-shape and quadratic relaxation factor, see Fig 3.12 left. On the right panels of this figure are outputs from two runs with the same initial conditions, but with different relaxation factors. As we can see, the sine-shaped factor provides a much smoother transition to the relaxation zone: compare right top and bottom figures. This scheme gave much better results in the latter runs than the linear boundary factor. The quadratic relaxation factor was used in the tests of the landuse dataset, and was kept in the present formulation of the lateral boundary condition.

To ensure *all* large frequency disturbances have been removed from the model, time variation of each variables in one single gridpoint (in the middle of the domain) were displayed. The remains of any possible large frequency noises should appear on such diagram (for example Fig 2.4 top). The only systematic large frequency noise is one with a period of 20 timestep. This is the result of the applied numerical scheme: an Euler forward scheme is used every 20 step to adjust the computational mode to the physical mode. The magnitude of this noise is negligible in all cases. Time variation of wind velocity components close to the ground (20m) shows very similar behavior to those obtained from other models [e.g., Kessler, 1982, Fig 2.4 bottom] which satisfies Pielke's second criterion of model evaluation.

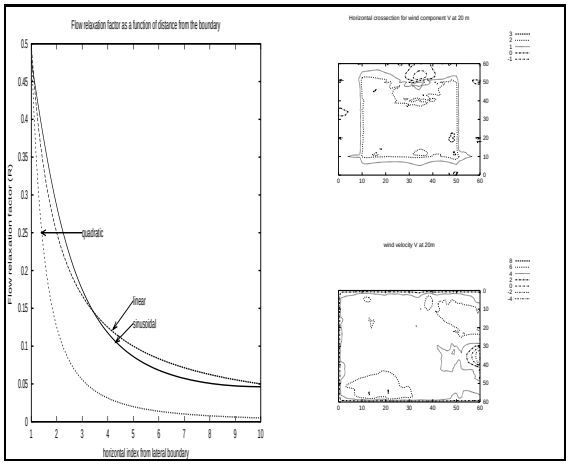

Figure 3.12: **The boundary relaxation factor (left) wind cross-section from calculations using linear (right top) and sine-shaped relaxation factor (right bottom)**

It also can be seen on these diagrams that within the first hour of integration some oscillation occurs according to the initialization processes. It's obvious that after 100-150 timesteps these fluctuations vanish. There are two possible reasons for such damping:

- Dissipation, due to too large a viscosity value
- An internal balance, developed by the model dynamics

If the first reason is responsible for the lack of large frequency noises, than the model must be overdamped. If the second is the possible reason, we can say that the model is suitable for dynamic initialization. To locate the reason of this damping the time variation of the model energies must be investigated. If the model is overdamped, the kinetic energy should decrease continuously. On the other hand systematic increase of the model energy is an indicator of a possible instability. Thus the investigation of the energies is a useful diagnostic tool to examine the fidelity of the model [Pielke, 1984].

On Fig 3.13 top two different kind of energies are plotted. Kinetic energy of the model is defined as:

$$K := \int_{\Omega} \varrho v^2 \, dV$$

where ϱ is the density of air, $v^2 = \mathbf{v} \cdot \mathbf{v}$ and $\Omega \in \Re^3$ denotes the whole model domain. The Convective

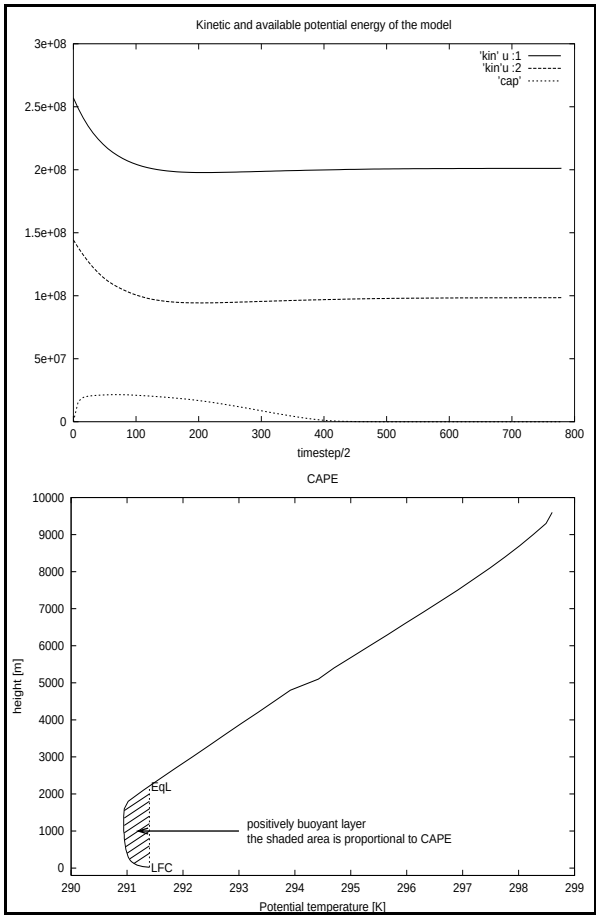

Figure 3.13: **Top: The model energies. Bottom: For the calculation of CAPE**

Available Potential Energy (CAPE) is the integral of the parcel buoyancy in the vertical direction for the positively buoyant layer (i.e., from the level of free convection (LFC) to the Equilibrium Level or Limit of Convection (EqL). On Fig 3.13 bottom the shaded area is proportional to the CAPE. In the calculation CAPE was determined using the following formula:

$$CAPE := \int_D \int_{z=z_{LFC}}^{z=z_{EqL}} \frac{g}{\Theta} \Delta\theta(z) \, dz$$

where g is acceleration due to gravity ($9.81[ms^{-1}]$) Θ is averaged potential temperature for the model domain, $\Delta\theta(z)$ is $\theta_{liftedparcel} - \theta_{environment}$ (convection is assumed to be adiabatic process ($\theta_{liftedparcel} = const.$) and $D \in \Re^2$ is the model domain in the horizontal (x–y) plain. CAPE is used to obtain the vertical velocity scale ($w_{CAPE} = \sqrt{2 \cdot CAPE}$) assuming that *all* potential energy is

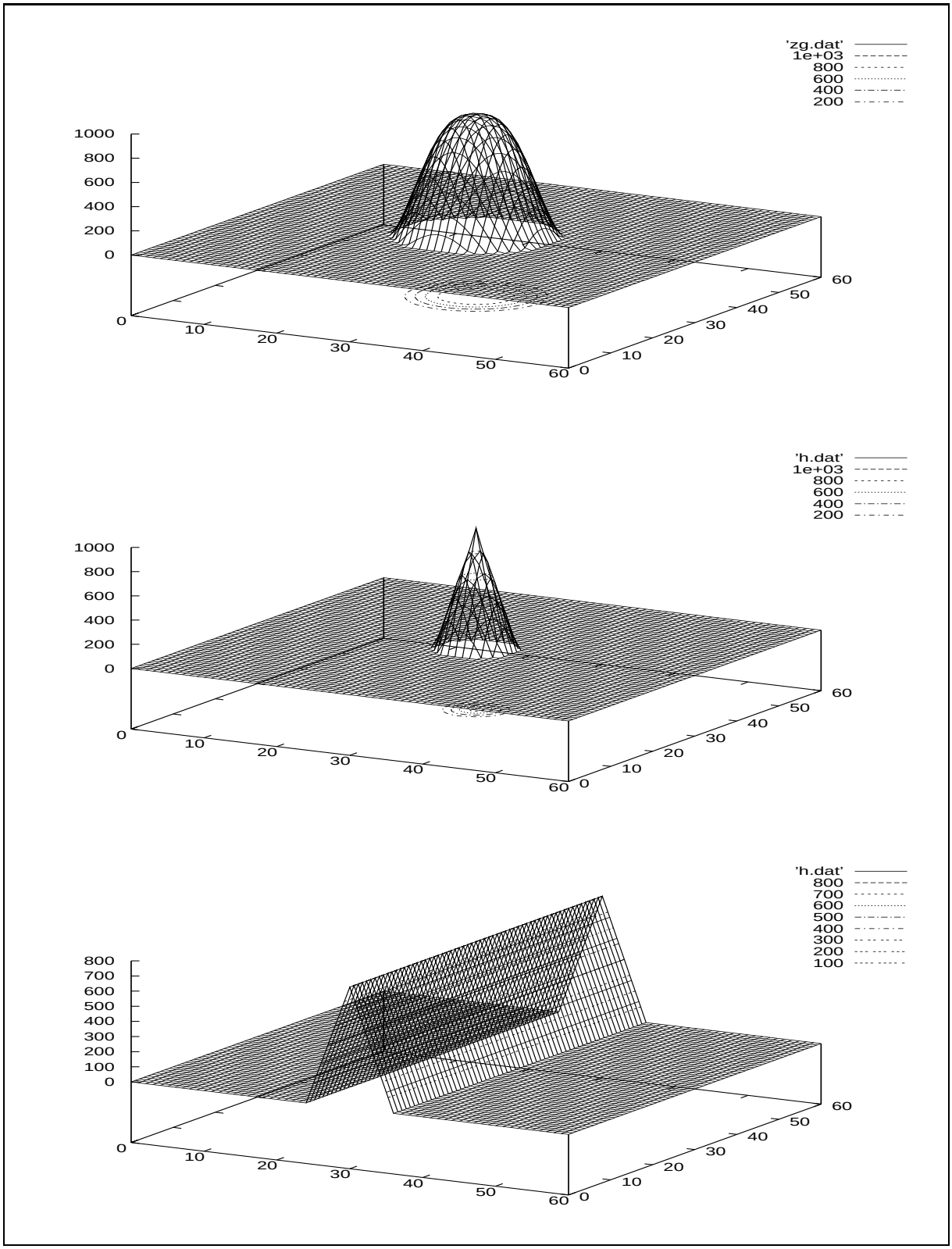

Figure 3.14: **Variations in artificial topography for the evaluation of the influence of topography**

converted into kinetic energy [Rogers *et al.*, 1985]. In the spin-up time (first 2 hours) the kinetic energy is decreasing logarithmically. As the model parameters reach their steady state value and dynamical balance is generated, there is a short period when the kinetic energy is slightly increasing, after which it is fairly constant. There is no significant change in it's value. These facts prove that an internal mesoscale balance is responsible for the relaxation of the initial noises. It is also an indicator of the numerical stability of the model, otherwise it should increase continuously.

Fig 3.12 right shows that the largest deviations of the flow are still in this relaxation zone near the lateral boundary. There are two possible way to find out if the topography or the possibly still not adequate boundary is generating such noises:

- The model domain should be enlarged at least 4 times greater, and the lateral boundaries should be removed far from the ridges of the Carpathian Mountains. This has enormous costs, which is beyond our computational facilities.
- A less expensive way to investigate the effect of the topography is to use an artificial topography database: simple uniform topography (isolated hill or ridge) in the center of the domain. This is much more economical, and the results can be evaluated through comparison with other model results, as this test was performed by nearly all modelers in the evaluation of their models.

The second method was chosen, and the results were compared to other model outputs. Three main cases were investigated. In the first case, bell-shaped hill was taken in the center of the domain. [Fig 3.14 top]. The surface of this hill was determined using the following formula:

$$z_g = \begin{cases} z_{max} - \frac{z_{max} r}{2R}(1 - \cos(\frac{r\pi}{R})) & \text{if } r \leq R \\ 0 & \text{otherwise} \end{cases}$$

where z_{max} is the elevation of the hill-top ($1000\,m$) R is the radius of the hill ($100\,km$) and r is the distance from the center of the domain. In the second case a cone-shape hill was considered (Fig 3.14 middle) to examine the effect of a sharp mountain peak. The third run was performed above a mountain ridge perpendicular to the direction of the main flow (Fig 3.14 bottom). All three runs resulted in numerically stable and realistic solutions. Time variation of some variables and the model energies were plotted to prove visually the lack of any instability or false wave patterns. The model seemed to be free from any large frequency waves even in the case of sharp peak or ridge. Model results were evaluated by qualitative comparison with other model results [with hydrostatic [Klemp and Lilly, 1978] and non-hydrostatic [Durran, 1981] simulations of flow over mountains]. Though these simulations were performed at stronger large-scale synoptic wind and stable stratification ($\partial_z\theta = 4\ K/km$) in the whole layer (in our simulations stratification were neutral up to 1000 m, and stable $\partial_z\theta = 4\ K/km$ above) our hydrostatic model gave almost identical results (see Fig 3.15). Fidelity of the model results for simple uniform cases is necessary but not sufficient evidence to prove the fidelity of the model over more general complex structures. The accuracy of the model dynamics for the latter case should be studied through comparison of the model results with observations and may depend on future works.

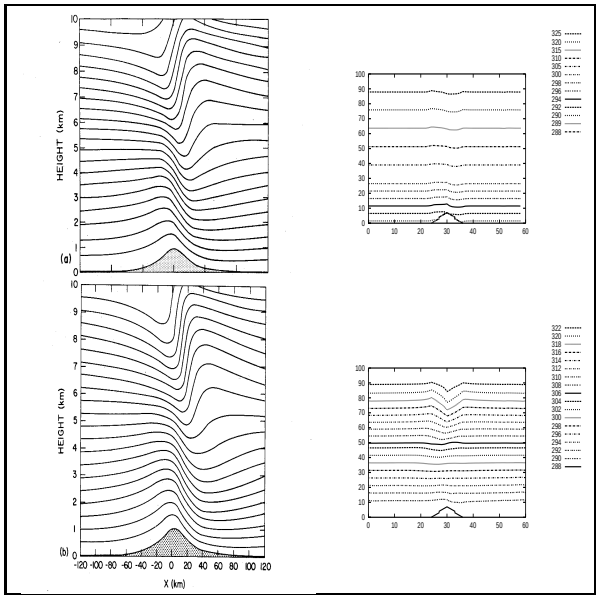

Figure 3.15: **Model evaluation of flow over obstacles: Left: Hydrostatic (top) and non-hydrostatic (bottom) simulations of other models. Right: flow over a cone-shaped isolated hill (top) and ridge (bottom). Contours of potential temperature are plotted on all figures.**

3.4 The Landuse Database

As already mentioned in the introduction of this chapter and in Section 2.3, the accuracy of the lower boundary condition is essential for a mesoscale model. Mesoscale circulations are strongly thermally induced, generated or influenced by the horizontal variation of the model variables in the surface layer. (e.g., sea or lake breezes, urban circulations, etc). The values of those variables are obtained from surface parameters, using parameterizations described in the model description. For this reason, it is essential that parameters defining the land cover landuse should be given precisely for the sake of the fidelity of a mesoscale model. These parameters can be obtained by using a land cover database prescribing a certain value for each parameters for every category in the land cover information. The land cover dataset was generated from the global land cover characteristics data base. The Lambert Azimuthal Equal Area projection has 1km nominal resolution and based on 1 km AVHRR data. The IGBP[8] Land Cover Classification [Belward, 1996] was used, which has the following 17 categories:

1. Evergreen Needleleaf Forest
2. Evergreen Broadleaf Forest
3. Deciduous Needleleaf Forest
4. Deciduous Broadleaf Forest
5. Mixed Forest
6. Closed Shrublands
7. Open Shrublands
8. Woody Savannas
9. Savannas
10. Grasslands
11. Permament Wetlands
12. Croplands
13. Urban and Built-Up
14. Cropland/Natural Vegetation Mosaic
15. Snow and Ice
16. Barren or Sparsely Vegetated
17. Water Bodies

[8] International Geosphere Biosphere Program

The spatial frequency distribution of each categories in the domain of the standard run are presented on Fig 3.16. As it can be seen, some categories have much greater significance than others (e.g., nor 16th neither 17th categories appear in the domain). As described in the description of the surface layer equations (in Section 2.2), the following external surface parameters are needed for the calculation:

1. albedo (α, non-dimensional)
2. roughness length (z_0 $[m]$)
3. thermal diffusivity ($K_g = v/\varrho_g [m^2 s^{-1}]$, where v is thermal conductivity $[Jkg^{-1}K^{-1}]$ and ϱ_g is density of the soil $[kg\,m^{-3}]$)
4. volmetric heat capacity ($C = c_g \varrho_g$ $[Jm^{-3}K^{-1}]$, where c_g $[Jkg^{-1}K^{-1}]$ is specific heat capacity and ϱ is density of the soil)
5. canopy conductance (Gs $[ms^{-1}]$)
6. coefficients for the calculation of the photosynthesis (a $[m^2W^{-1}]$, b $[mg\,CO_2\,m^2s^{-1}]$)

Originally, 13 categories were considered for the landuse parameters (1–4 items in the above list), while 15 categories were considered in the vegetation categories (items 5–6). The 13 landuse categories were:

1. Sea
2. Evergreen Broadleaf
3. Evergreen Coniferes
4. Deciduous Coniferes
5. Deciduous Broadleaf Forest
6. Evergreen Broadleaf Forest
7. Mixed Forest
8. Temperate Grassland
9. Bog
10. Arable Cropland
11. Rice
12. Urban
13. Water

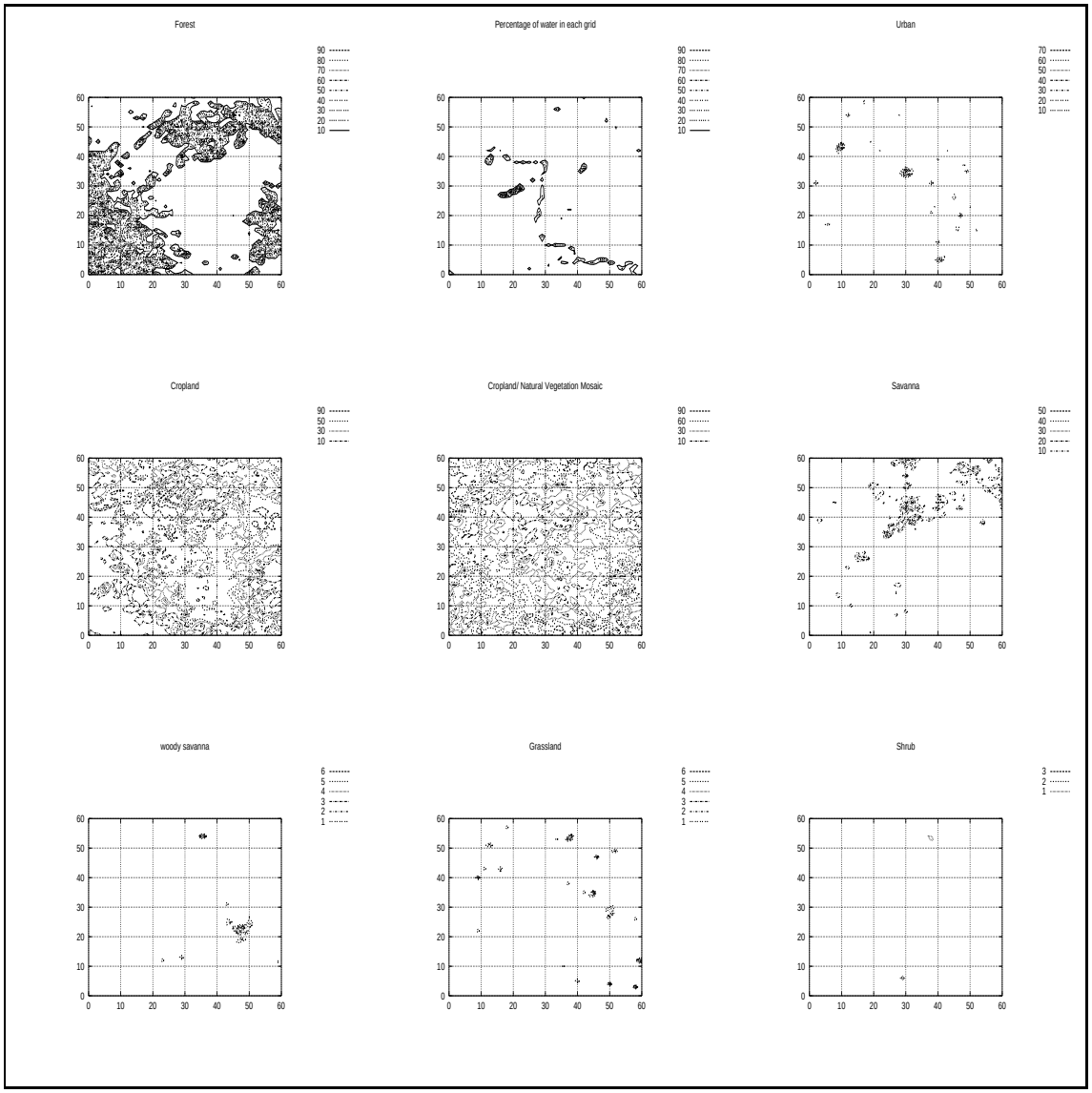

Figure 3.16: **Spatial frequency distribution of each category of land cover**

For vegetation the next categories were used for Japan:

1. Rice Field
2. Arable Land
3. Orchards
4. Trees
5. Forest
6. Wasteland
7. Buildings
8. Houses
9. Main Traffic
10. Other Artificial Use
11. Lakes
12. River
13. River Side
14. Sea Shore
15. Unknown

The landuse and land cover data bases both contain 17 categories now, as the IGBP dataset. In Appendix C on Table C.1 the concordance of the present datasets to the original ones are presented. For the categories Savannas, Grassland, Snow and Ice and Barren or Sparsely Vegetated there were no concording values in the original dataset. Though the two latter categories are not present in the domain of the standard run, for the sake of universality of the model, i.e., be suitable for other locations, it's necessary to prescribe realistic values for these categories, too. Table C.2 shows the values of each parameter for these categories. In this table those parameters not taken from Stull were obtained from measurements by Lee (1978, page 84). Snow and Ice parameters have a wide range. For example, albedo ranges from 0.2-0.95 in the literature. Here, for simplicity, albedo was put equal to 0.4. Albedo and roughness length data for desert were used for the category Barren and Sparsely Vegetated. Thermal diffusivity and heat capacity were obtained using the corresponding data of rock. As the number of categories have been changed, some changes were to be made even in the source code of the model. Some test runs were performed to prove the fidelity of the new, Hungarian version of the NRIPR mesoscale model.

3.5 Concluding Remarks

The NRIPR mesoscale model has been adapted and tested for use in Central Europe. The topography, landuse and vegetation datasets were generated, the boundary conditions have been modified to perform suitable runs, even in a basin, where the model domain is surrounded by relatively high mountains. The parameterizations have been modified according to the new land cover landuse datasets. The model has been tested. It's sensitivity have been checked with respect to both the model dynamics and the surface parameters. These tests, after the adaptation produced dynamically stable and realistic results for arbitrary initial conditions. Further tests should be made to evaluate the model for realistic initial conditions. It can be nested into a regional LAM (e.g., Aladin). Implementation of the CO_2 version of this model includes the adaptation of some additional datasets (information of large stacks, anthropogenic heat flux, anthropogenic carbon-dioxide emission, etc).

As already mentioned in Section 2.3 the water vapor and phase changes in the atmosphere should be dealt more precisely in the model. In an air quality model precipitation has a great importance. Parameterization of clouds (both mesoscale and subgrid-scale clouds) and precipitation should be included through the proper parameterizations.

By adding some other parameterizations of other pollutants, (chemistry package) the model can be used to assess the concentrations of any pollutants in the atmosphere. This can be useful in the assessment of new air quality standards, and in helping governments and business companies develop strategies for planning new industrial plants. Accuracy of the model can be increased with the application of parameterizations of convective clouds or precipitation, for example. The meteorological outputs of such a model can be used to generate wind climatologies of a certain region, which is an essential step in wind energy planning. Before organizing a field experiment, numerical experiments should be made at the considered area with high resolution, so as to optimize the expedition. Numerical simulation of a field experiment can help to find the most interesting sites of the considered area (where to put the instruments). Numerical experiments are less expensive, compared to a field experiment, since they can be repeated for any initial and boundary conditions, to study one particular phenomenon. After the expedition, some unmea-

sured parameters can be calculated by running the model with the measured data as initial and boundary conditions. Finally, this model can be a powerful tool even for theoretical research. The investigated phenomenon can be studied both in idealized conditions, separately as it cannot be observed in the atmosphere, and in it's complex environment, which is impossible analytically.

3.6 Acknowledgement

This paper was written at Uppsala University, Sweden. The writer has been there on a scholarship from the European Union in the framework of the ERASMUS program, for three months. The Department of Earth Sciences, Meteorology at Uppsala University (MIUU) provided in an inspiring environment theoretical and technical tools for it. The author wishes to express his sincere thanks to Dr. Leif Enger, associate professor, leader of the modeling group at Uppsala University, for his kind help and for the fact that he provided the needed datasets for the calculations, and gave the opportunity to use rainbow SGI system for the numerical runs.

Special thanks to Dr Dezső Dévényi, FSL NOAA Boulder, Colo., for his much advise and great help.

Many thanks to Mathias Mohr (MIUU) for fruitful discussions and for his technical help. The author would like to acknowledge Zoltán Barcza Deptartement of Meteorology at Eötövs University, Budapest, Hungary, for his help in solving informatics problems, Scott Krayenhoff, University of British Columbia, Canada, for his correction and comments on the English manuscript.

Finally, and most importantly, I would like to acknowledge my supervisors, Dr. Zsuzsanna Iványi and Dr. Tamás Weidinger, Department of Meteorology at Eötvös University, Budapest Hungary, who gave me the opportunity to deal with such an interesting area.

REFERENCES

Anthes, R.A., Warner, T.T., 1978: Development of hydrodynamic models suitable for air pollution and other meteorological studies, *Month. Weather Rev.*, **106**, 1045-1078

Arakawa, A., 1966: Computational Design for Long-Term Numerical Integration of the Equation of Fluid Motion: Two-Dimensional Incompressible Flow. Part I., *J. Comp. Phys.*, **1**, 119-143

Arakawa, A., 1972: Design of the UCLA general circulation model, Technical report No. 7; Numerical simulation of weather and climate, Department of Meteorology, UCLA

Belward, A.S., ed., 1996: The IGBP-DIS[9] global 1km land cover dataset (DISCover)-proposal and implementation plans: IGBP-DIS Working Paper No. 13, Toulouse, France, 61 pp

Bonner, W.D., 1968: Climatology of the low-level jet. *Month. Weater Rev.*, **96**, 833-850

Briere, S., 1982: Nonlinear normalmode initialization of a limited area model, *Month. Weather Rev.*, **110**, 1166-1186

Daley, R., 1991: Atmospheric Data Analysis. Cambridge University Press, Cambridge, 457 pp

Davies, H.C., 1975: Lateral boundary formulation for multi-level prediction model. *Quart. J. R. Met. Soc.*, **102**, 405-418

Durran, D.R., 1981: The effect of Moisture on Mountain Lee Waves. NCAR Cooperative PhD Thesis No. 65 with the Massachusetts Institute of Technology

Emanuell, K., 1983: On the dynamic definition of mesoscale. *Mesoscale Meteorology: Theory, observation and models*, D., Lilly and T., Gal-Chen, eds., Dordrecht, Reidel

Enger, L., Grisogono, B., 1988: The response of bora type flow to sea surface temperature. *Q. J. R. Meteorol. Soc.*, **124**, 1227-1244

Estoque, M.A., 1961: A theoretical investigation of the sea breeze. *Q. J. R. Meteorol. Soc.*, **87**, 136-146

Gambo, K., 1978: Notes on the turbulence closure model for atmospheric boundary layers *J. Meteor. Soc. Jpn.*, **56**, 466-480

Gustafsson, N., Källen, E., Thorsteinsson, S., 1998: Snsitivity of forecast errors to initial and lateral boundary conditions. *Tellus*, **50A**, 167-185

Hove, J.E., Anthes, R.A., 1976: The initialization of numerical models by a dynamic initialization technique. *Mon. Weather Rev.*, **108**, 1010-1028

Klemp J.B., Lilly. D.K., 1975: The dynamics of the wave induced downslope winds. *J. Atmos. Sci.*, **32**, 320-339

Klemp, J.B., Lilly, D.K., 1978: Numerical simulation of hydrostatic mountain waves. *J. Atmos. Sci.*, **32**, 78-107

Kondo, H., 1986: A numerical Experiment about the cooling in a small basin, *J. Meteor. Soc. Jpn.*, **64**, 563-574

Kondo, H., 1989: Description of the NRIPR mesoscale meteorological model, Report of the NRIPR, No. 44, 76 pp

Kondo, J., 1975: The course of atmospheric science I, Atmosphere near the surface, University Press of Tokyo University, 226 pp

Kondo, J., 1976: Effect of radiative heat transfer on profiles of wind, temperature and water vapor in the atmospheric boundary layer, *J. Meteor. Soc. Jpn.*, **49**, 75-94

Lee, R., 1978: Forest meteorology, Columbia University Press, New York Estoque, M.A., 1961: A theoretical investigation of the sea breeze *Q. J. R. Meteorol. Soc.*, **87**, 136-146

Ligda, M.G.H., 1951: Radar Storm Detection Compendium of Meteorology (Melone, T.F., ed.) American Meteorological Society, Boston 1265-1282

Houze, R.A., Hobbs, P.V., 1982: Organization and structure of the precipitation cloud systems. *Adv. Geophys.*, **24**, 225-315

McPherson, R.D., 1970: A numerical study of the effect of a costal irregularity on the sea breeze, *J. Appl. Meteorol.*, **9**,

[9]Data Information System

776-777

Mahrer, Y., Pielke, R.A., 1977: The effect of topography on the sea and land breezes in a two dimensional numerical model. *Mon. Wea. Rev.*, **105**, 1151-1162

Manins, P.C., 1981: A numerical simulation of nocturnal drainage flow. *J. Meteorol. Soc. Jpn.*, **59**, 108-122

Manins, P.C., Sawford, B.L., 1979: A model of katabatic winds. *J. Atmos. Sci.*, **36**, 619-630

Mannouji, N., 1982: A Numerical experiment on the mountain and valley winds, *J. Meteor. Soc. Jpn.*, **60**, 1085-1105

Mellor, G., Yamada, T., 1974: A hierarchy of turbulent closure models for planetary boundary layers, *J. Atmos. Sci.*, **31**, 1792-1806

Monin, A.S., and Obukhov, A.M., 1954: Basic lows of turbulent mixing in the atmosphere near the ground. *Tr. Akad. Nauk. SSSR Geophiz. Inst.*, No.**24** (151) 1963-1984

Morse, B.J., 1973: An Analytical Study of the Mesh Refinement Applied to the Wave Equation. NOAA Technical Memorandum WMPO-5, August 1973

Oke, T.R., 1978: Boundary Layer Climates. Halsted Press, NY 372 pp

Oliger, J., and Sundström, A., 1976: Theoretical and Practical Aspects of Some Initial-boundary Value Problems in Fluid Dynamics. Report STAN-CS-76-578, Stanford University, Computer Science Department

Orlanski, I., 1975: A rational subdivision of scales for atmospheric processes. *Bull. Amer. Meteor. Soc.*, **56**, 529-530

Orlanski, I., 1976: A simple boundary condition for unbounded hyperbolic flows. *J. Comput. Phy.*, **21**, 251-269

Orlanski, I., 1984: Scale analysis and equations of motion for mesoscale. Draft manuscript prepared for a nordic course on Mesoscale Meteorology, Pinnarpsbaden, Sweden, May 30-June 10 1983. Organized by Swedish Meteorological Society, to be published

Pielke, A.R., 1984: Mesoscale Meteorological Modeling, Academic press, INC. Orlando, Florida 612 pp

Rogers, D.P., Telford, J.W., and Chai, S.K., 1985: Entrainment and the temporal development of the microphysics of convective clouds. *J. Atmos. Sci.*, **42**, 1846-1858

Stull, R.B., 1988: An Introduction to Boundary Layer Meteorology, Kluwer Academic Publishers, Dordrecht, 666 pp

Takano, K., 1976: Three dimensional numerical modeling of the land and sea breezes and the urban heat island in the Kanto plain Dr. Sci. Thesis, University of Tokyo

Thunisvariation of potential temperature in addition to d, P., Bornstein, R., 1997: Hierarchy of Mesoscale Flow Assumptions and Equations. *J. Atmos. Sci.*, **53**, 380-397

Warner, T.T., Peterson, R.A., Russell, E.T., 1997: A Tutorial on Lateral Boundary Conditions as a Basic and Potentially Serious Limitation to Regional Numerical Weather Prediction, *Bull. Amer. Meteor. Soc.*, **78**, 2599-2616

Wong, R.K.W., Hage, K.D., 1983: Comment on the Terrain Following Coordinate and the Hydrostatic Approximation, *J. Atmos. Sci.*, **40**,2875-2878

Yamada, T., 1981: A numerical simulation of nocturnal drainage flow. *J. Meteorol. Soc. Jpn.*, **59**, 108-122

Yoshizaki, M., 1988: Manual for ORT-UT convection model. Manual for a numerical experiment about the precipitation forced by topography

Appendix A

The Model Equations

A.1 The Hydrostatic Equation

The Hydrostatic Equation can be derived from the third equation of motion: neglecting the Coriolis and frictional forces:

$$\frac{dw}{dt} = -\frac{1}{\varrho}\frac{\partial p}{\partial z} - g$$

On the mesoscale the ratio of the vertical acceleration to the pressure gradient term is usually much less than unity [a representative value of this ratio is 0.0003 (Pielke, 1984)]. In that case, the vertical acceleration term can be neglected[1], an assumption that yields the hydrostatic equation:

$$-\frac{1}{\varrho}\frac{\partial p}{\partial z} = g$$

Substituting the Equation of State of Ideal Gas ($\frac{1}{\varrho} = \frac{RT}{p}$) and introducing the potential temperature, defined by:

$$\theta = T(\frac{p_{00}}{p})^{R_d/c_p}$$

and the scaled pressure (or Exner function):

$$\pi = c_p(\frac{p}{p_{00}})^{R_d/c_p}$$

where T is absolute temperature, p is pressure, p_{00} is a reference value for pressure (usually taken to 1000 mbar), R_d is specific gas constant of dry air, c_p is specific heat capacity on constant pressure, yields the hydrostatic equation in the scaled pressure form:

$$\theta\frac{\partial \pi}{\partial z} = -g \tag{A.1}$$

It is convenient to define a large-scale average for both pressure (Π) and temperature (Θ), such that the left side of Eqn A.1 is in exact balance with the gravity force:

$$\Theta\frac{\partial \Pi}{\partial z} = -g \tag{A.2}$$

The instantaneous value of these variables can be split into large-scale mean value and mesoscale deviation:

$$\theta = \Theta + \theta'$$

$$\pi = \Pi + \pi'$$

[1] This assumption is referred to as hydrostatic assumption in the text

Using this notation the hydrostatic equation (Eqn A.1) can be written as:

$$\Theta\frac{\partial\Pi}{\partial z}+\theta'\frac{\partial\Pi}{\partial z}+\Theta\frac{\partial\pi'}{\partial z}+\theta'\frac{\partial\pi'}{\partial z}=-g$$

As on the large-scale an exact equilibrium is assumed (Eqn A.2); the first term on the right hand side is precisely equal to the left hand side. The second term can be written as $-g\frac{\theta'}{\Theta}$, which is an expression for buoyant forces. Neglecting the second order deviation yields a diagnostic expression for the mesoscale deviation of the scaled pressure:

$$\Theta\frac{\partial\pi'}{\partial z}=g\frac{\theta'}{\Theta} \tag{A.3}$$

This equation is in the set of the model's governing equations. The primes ($'$) in the notation of mesoscale pressure and temperature are dropped in the text for the sake of simplicity.

Note that in the prognostic equation of horizontal motion,the large-scale pressure gradient terms are expressed with the gradient wind components, using the geostrophic relationship ($(u_g,v_g)=\frac{1}{f\varrho}(-\frac{\partial p}{\partial y},\frac{\partial p}{\partial x})$),and terms containing the temperature deviation (θ) are neglected.

A.2 The governing equations in the terrain following system

Using the chain rule of calculus and the definition of the new vertical coordinate (Eqn 2.6.) the governing equations (2.1)-(2.5) are written as follows:

$$\frac{\partial}{\partial x}(Du)+\frac{\partial}{\partial y}(Dv)+\frac{\partial}{\partial s}(D\dot{s})=0 \tag{A.4}$$

$$\begin{aligned}&\frac{\partial}{\partial t}(Du)+\frac{\partial}{\partial x}(Du^2)+\frac{\partial}{\partial y}(Duv)+\frac{\partial}{\partial s}(Du\dot{s})-fD(v-v_g)=\\&-\Theta D(\frac{\partial\pi}{\partial x}-(s-1)\frac{\partial D}{\partial x}\frac{g\theta}{\Theta^2})+K_H^uD\frac{\partial^2u}{\partial x^2}+K_H^uD\frac{\partial^2u}{\partial y^2}-\frac{1}{D}\frac{\partial}{\partial s}(K_V^u\frac{\partial u}{\partial s})\end{aligned} \tag{A.5}$$

$$\begin{aligned}&\frac{\partial}{\partial t}(Dv)+\frac{\partial}{\partial x}(Duv)+\frac{\partial}{\partial y}(Dv^2)+\frac{\partial}{\partial s}(Dv\dot{s})+fD(u-u_g)=\\&-\Theta D(\frac{\partial\pi}{\partial y}-(s-1)\frac{\partial D}{\partial y}\frac{g\theta}{\Theta^2})+K_H^uD\frac{\partial^2v}{\partial x^2}+K_H^uD\frac{\partial^2v}{\partial y^2}-\frac{1}{D}\frac{\partial}{\partial s}(K_V^v\frac{\partial v}{\partial s})\end{aligned} \tag{A.6}$$

$$\frac{\partial\pi}{\partial z}=\frac{g\theta'}{\overline{\Theta}^2}D \tag{A.7}$$

$$\begin{aligned}&\frac{\partial}{\partial t}(D\theta)+\frac{\partial}{\partial x}(Du\theta)+\frac{\partial}{\partial y}(Dv\theta)+\frac{\partial}{\partial s}(D\theta\dot{s})=\\&K_H^\theta\frac{\partial^2\theta}{\partial x^2}-K_H^\theta(s-1)\frac{\partial\theta}{\partial s}\frac{\partial^2}{\partial x^2}(\log D)-K_H^\theta\frac{\partial\log D}{\partial x}(s-1)\frac{\partial}{\partial s}\frac{\partial\theta}{\partial x}\\&+K_H^\theta\frac{\partial^2\theta}{\partial y^2}-K_H^\theta(s-1)\frac{\partial\theta}{\partial s}\frac{\partial^2}{\partial y^2}(\log D)-K_H^\theta\frac{\partial\log D}{\partial y}(s-1)\frac{\partial}{\partial s}\frac{\partial\theta}{\partial y}\\&+\frac{1}{D}\frac{\partial}{\partial s}(K_V^\theta\frac{\partial\theta}{\partial s})+\frac{\partial F}{\partial z}\end{aligned} \tag{A.8}$$

Here, $\dot{s}=(w-\frac{\partial z}{\partial t}-u(\frac{\partial z}{\partial x})-v(\frac{\partial z}{\partial y}))\frac{\partial s}{\partial z}$), and w is vertical velocity in the Cartesian system. Note that in the diffusion term the effect of the slopping terrain is considered only in the equation for potential temperature (Eqn A.8)

Appendix B

Finite Difference Scheme

B.1 The Arakawa Scheme

The finite difference analogues of the advection terms in Equation A.5 are written as follows:

$$\begin{aligned}
&0.5[\{F_{i+\frac{1}{2},j,k}(u_{i+\frac{1}{2},j,k}+u_{i,j,k})-F_{i-\frac{1}{2},j,k}(u_{i,j,k}+u_{i-1,j,k})\\
&+G_{i,j+\frac{1}{2},k}(u_{i,j+1,k}+u_{i,j,k})-G_{i,j-\frac{1}{2},k}(u_{i,j,k}+u_{i,j-1,k})\\
&+\tilde{F}_{i+\frac{1}{2},j+\frac{1}{2},k}(u_{i+1,j+1,k}+u_{i,j,k})-\tilde{F}_{i-\frac{1}{2},j-\frac{1}{2},k}(u_{i,j,k}+u_{i-1,j-1,k})\\
&+\tilde{G}_{i-\frac{1}{2},j+\frac{1}{2},k}(u_{i-1,j+1,k}+u_{i,j,k})-\tilde{G}_{i+\frac{1}{2},j-\frac{1}{2},k}(u_{i,j,k}+u_{i+1,j-1,k})\}\\
&+0.5\{S_{i,j,k+\frac{1}{2}}(u_{i,j,k+1}+u_{i,j,k}-S_{i,j,k-\frac{1}{2}}(u_{i,j,k}+u_{i,j,k-1}-)\}]/\Delta x\Delta y
\end{aligned}$$

Here

$$F_{i+\frac{1}{2},j,k}=\frac{1}{6}(F^*_{i+\frac{1}{2},j+1,k}+2F^*_{i+\frac{1}{2},j,k}+F^*_{i+\frac{1}{2},j-1,k})$$

$$G_{i,j+\frac{1}{2},k}=\frac{1}{6}(G^*_{i+\frac{1}{2},j,k}+G^*_{i+\frac{1}{2},j+1,k}+G^*_{i-\frac{1}{2},j,k}+G^*_{i-\frac{1}{2},j+1,k})$$

$$\tilde{F}_{i+\frac{1}{2},j+\frac{1}{2},k}=\frac{1}{12}(G^*_{i-\frac{1}{2},j,k}+G^*_{i+\frac{1}{2},j+1,k}-F^*_{i+\frac{1}{2},j,k}-F^*_{i+\frac{1}{2},j+1,k})$$

$$\tilde{G}_{i-\frac{1}{2},j+\frac{1}{2},k}=\frac{1}{12}(G^*_{i-\frac{1}{2},j,k}+G^*_{i-\frac{1}{2},j+1,k}-F^*_{i-\frac{1}{2},j,k}-F^*_{i-\frac{1}{2},j+1,k})$$

For S the following formula is used to satisfy continuity equation:

$$\begin{aligned}
S_{i,j,k+\frac{1}{2}}=\frac{1}{8}(&\dot{s}_{i+\frac{1}{2},j+1,k+\frac{1}{2}}+\dot{s}_{i-\frac{1}{2},j+1,k+\frac{1}{2}}+\dot{s}_{i+\frac{1}{2},j-1,k+\frac{1}{2}}+\dot{s}_{i-\frac{1}{2},j-1,k+\frac{1}{2}}\\
&+2(\dot{s}_{i+\frac{1}{2},j,k+\frac{1}{2}}+\dot{s}_{i-\frac{1}{2},j,k+\frac{1}{2}}))
\end{aligned}$$

F^* and G^* are defined in the same gridpoint as potential temperature. $\dot{s}$ is defined at the same gridpoint as potential temperature on the projection of iso-s plane, and vertically staggered with θ.

$$F^*_{i+\frac{1}{2},j,k}=\frac{1}{4}\{(D_{i+\frac{1}{2},j}+D_{i+\frac{3}{2},j})u_{i+1,j,k}+(D_{i+\frac{1}{2},j}+D_{i-\frac{1}{2},j})u_{i,j,k}\}$$

$$G^*_{i+\frac{1}{2},j,k}=\frac{1}{4}\{(D_{i+\frac{1}{2},j}+D_{i+\frac{1}{2},j+1})v_{i+\frac{1}{2},j+\frac{1}{2},k}+(D_{i+\frac{1}{2},j}+D_{i+\frac{1}{2},j-1})u_{i+\frac{1}{2},j-\frac{1}{2},k}\}$$

A similar method is used for the v component and for θ, but with u replaced by v and θ, respectively.

B.2 The Horizontal Diffusion Term

In this section, vertical indices are neglected for the sake of simplicity, as horizontal diffusion terms are all considered for the same vertical indices. Finite difference scheme for diffusion of u:

$$K_H^u(u_{i+1,j} + u_{i-1,j} + u_{i,j+1} + u_{i,j-1} - 4u_{i,j})/\Delta^2$$

the same for v:

$$K_H^v(v_{i+1,j} + u_{i-1,j} + v_{i,j+1} + v_{i,j-1} - 4v_{i,j})/\Delta^2$$

and for θ:

$$K_H^\theta\{(s-1)[(\log D)_{i+1,j} + (\log D)_{i-1,j}(\log D)_{i,j+1} + (\log D)_{i,j-1} - 4(\log D)_{i,j}]T_{i,j} +$$

$$0.25(s-1)\{[(\log D)_{i+1,j} - (\log D)_{i-1,j}](T_{i+1,j} - T_{i-1,j}) +$$

$$[(\log D)_{i,j+1} - (\log D)_{i,j-1}](T_{i,j+1} - T_{i,j-1})\}\}/\Delta^2$$

where Δ is horizontal resolution, $\log D$ is the natural logarithm of the vertical extension of the model domain $z_T - z_G$ and

$$T_{i,j} = (\theta_{i,j,k+1} - \theta_{i,j,k-1})/2\Delta s$$

B.3 The Pressure Gradient Term

The vertical grid for π and Θ is staggered, so the scheme for the u pressure gradient term should be written:

$$\frac{1}{2}\theta D\{[(\pi_{i+\frac{1}{2},j,k-\frac{1}{2}} - \pi_{i-\frac{1}{2},j,k-\frac{1}{2}})/\Delta x$$

$$-\frac{1}{4}(s_{k-\frac{1}{2}} - 1)\frac{g}{\Theta^2}(\theta_{i+\frac{1}{2},j,k-1} + \theta_{i-\frac{1}{2},j,k-1} + \theta_{i+\frac{1}{2},j,k} + \theta_{i-\frac{1}{2},j,k})(D_{i+\frac{1}{2},j} - D_{i-\frac{1}{2},j})/\Delta x]$$

$$+[(\pi_{i+\frac{1}{2},j,k+\frac{1}{2}} - \pi_{i-\frac{1}{2},j,k+\frac{1}{2}})/\Delta x$$

$$-\frac{1}{4}(s_{k+\frac{1}{2}} - 1)\frac{g}{\Theta^2}(\theta_{i+\frac{1}{2},j,k+1} + \theta_{i-\frac{1}{2},j,k+1} + \theta_{i+\frac{1}{2},j,k} + \theta_{i-\frac{1}{2},j,k})(D_{i+\frac{1}{2},j} - D_{i-\frac{1}{2},j})/\Delta x]\}$$

Appendix C

Tables for the Landuse Land Cover Parameterizations

Present Category	Original Land Cover	Original Landuse
1. Evergreen Needleleaf	3. Evergreen Conifers	5. Forest
2. Evergreen Broadleaf	6. Evergreen Broadleaf	5. Forest
3. Deciduous Needleleaf	4. Deciduous Conifers	5. Forest
4. Deciduous Broadleaf	5. Deciduous Broadleaf	5. Forest
5. Mixed Forest	7. Forest	5. Forest
6. Closed Shrublands	2. Evergreen Broadleaf Shrubs	3. Orchards
7. Open Shrublands	2. Evergreen Broadleaf Shrubs	3. Trees
8. Woody Savannas	7. Forest	5. Forest
11. Permament Wetland	11. Rice	1. Rice Field
12. Croplands	10. Arable Cropland	2. Arable Cropland
13. Urban	12. Urban	7. Buildings
14. Natural Vegetation Mozaic	10. Arable Cropland	2. Arable Cropland
17. Water Bodies	13. Water	11. Lakes

Table C.1: **Concordance Table of the present landuse and land cover categories to the original classification**

Cathegory	α	z_0	K_g	C
9. Savannas	0.2*	0.1*	0.6	2.0
10. Grassland	0.2*	0.3*	0.5	2.0
15. Snow and Ice	0.4	10^{-4}*	1.0	1.3
16. Barren and Sparsely Vegetated	0.25	10^{-3}	1.4	6.8

Table C.2: **External parameters for the new categories**

*Taken from Stull (1988)

1. albedo (α, non-dimensional)
2. roughness length (z_0 $[m]$)
3. thermal diffusivity ($K_g = v/\varrho_g$ $[m^2 s^{-1}]$, where v is thermal conductivity $[Jkg^{-1}K^{-1}]$ and ϱ_g is density of the soil $[kg\, m^{-3}]$)
4. volmetric heat capacity ($C = c_g \varrho_g$ $[Jm^{-3}K^{-1}]$, where c_g $[Jkg^{-1}K^{-1}]$ is specific heat capacity of the soil)